Wireless Transceivers for Implantable Microsystems

by

Mohammad Hassan Ghaed

A dissertation submitted in partial fulfillment
of the requirements for the degree of
Doctor of Philosophy
(Electrical Engineering)
in The University of Michigan
2013

Doctoral Committee:

        Professor Dennis M. Sylvester, Chair
        Professor David Blaauw
        Assistant Professor Gary D. Luker
        Associate Professor David D. Wentzloff

I dedicate this dissertation to my wife, Sadaf.

Her love motivates every moment of my life.

TABLE OF CONTENTS

LIST OF FIGURES

LIST OF TABLES

CHAPTER 1

Introduction

1.1 Motivation and Background

There has been a significant amount of work on sensor nodes. Specifically, the works on implantable sensors for various cardiac[1], intraocular[2], and neural[3] applications have been promising. Although a wireless link can significantly simplify programming and usage of such microsystems, most of previously proposed systems lack a proper data link that is designed within energy, size, and range constraints of such systems. These three constraints shown in Figure 1.1 differentiate implantable biomedical transceivers from conventional radios used in other long and short-range applications [4]. In this section, we will investigate each of these three requirements to understand why none of previous solutions satisfies all of them simultaneously.

1.1.1 Energy and Peak Current Constraint

In order to provide continuous sensing, the implantable microsystem will need a reliable energy source. 1-10 mm^2 thin-film Li-ion batteries offer the only viable energy source for such systems. However, peak current of such batteries (10-$50\mu A$) is well below RF blocks (mA-range). The natural solution to this problem is to run the power-hungry radio off a capacitive charge reservoir for a short period. During this period, a small packet is transmitted. Afterwards, battery can recharge the charge reservoir to prepare for the transmission of the next bit. This way, we can trade off some bit-rate for lower peak power.
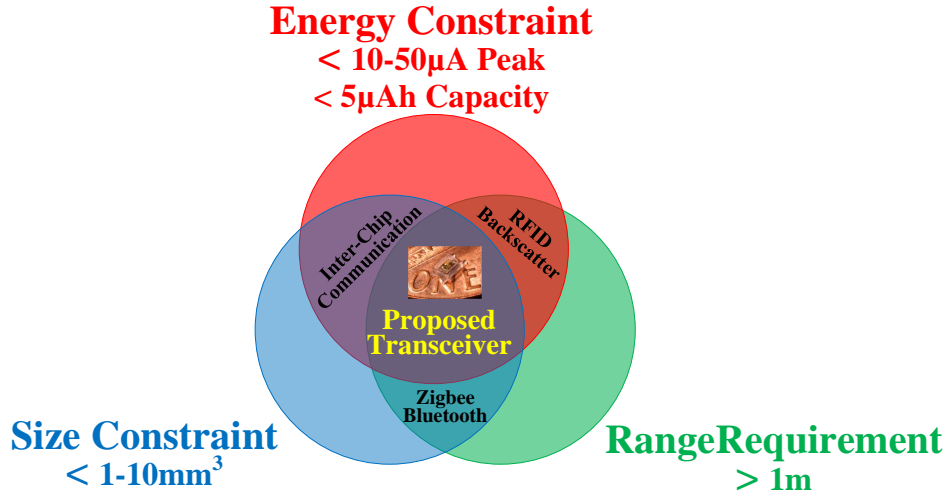
Figure 1.1: **The three major challenges for a transceiver targeted for implantable microsystems.**

Due to the peak current limitation, radio has to turn on, transmit a short packet while running off the capactive charge reservoir, and go back to sleep. Since only 1-10nF of MIM capacitor can fit in our mm^2 system, the whole radio on-period will be limited to few μs assuming 1mA-level radio power. As a result, conventional Non-Returning-to-Zero (NRZ) signaling, though spectrally efficient, is not feasible in this case. Figure 1.2 shows the time domain and Power Spectral Density (PSD) of NRZ and Manchester encoded signals. NRZ signaling that is widely used in wireline [5] and wireless [6] applications is difficult to recover clock from. Also, unless other encoding measures are used, long streams of "1"s and "0"s can pose more challenges in Clock and Data Recovery (CDR) process. For these reasons a synchronization stream is always required to guarantee low Bit-Error-Rate (BER). In mm^3 systems, however, short transmission window and startup issues make it impossible to include a synchronization pattern in every packet. As a result, although NRZ signaling achieves sub nJ/bit energies and high transmission ranges in standard radios like bluetooth [7] and IEEE 802.11 [8], it is not only unattractive, but also impossible to implement in this class of mm^3 devices targeted for biomedical applications.

Manchester encoding, as shown in 1.2, modifies the spectral content of transmitted signal by representing bit "1" with a rising edge and bit "0" with a falling edge. As a result, the CDR process is drastically simplified at the cost of reduced bitrate. This CDR simplification makes Manchester encoding a perfect candidate for compact microsystems where
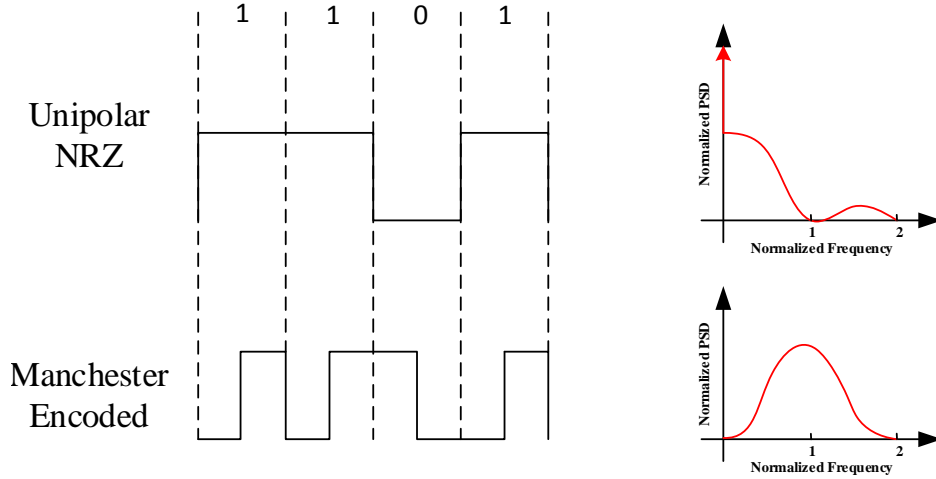
Figure 1.2: **NRZ and Manchester signaling comparison. NRZ signals are more spectrally efficient while Manchester encoded signals are easier from a synchronization perspective.**

total circuit area and power are highly limited. Besides, Manchester encoding eliminates the need for power-hungry accurate on-chip synthesizers required in conventional NRZ CDRs [9]. In Chapter 5, we will present a low-power receiver with Manchester decoding targeted at compact biomedical implants.

1.1.2 Size Constraint

Passive backscattering RFID radios have been widely used in low-power applications [10]. While these radios satisfy the energy and range requirement desired in mm^3 implants, their coil size (typically in cm range) prevents their use in such applications (Figure 1.1).

For active radios, integration of transceivers, more specifically CMOS transceivers, has resulted in solutions that are almost completely integrated. In this context, integrated active radios can be divided into two categories:

- **Standardized Far Field Radios:** Zigbee [11], WiFi [12], GSM [13] and CDMA [14] are some of the standards for which highly-integrated solutions have been proposed. The three components that are still typically not integrated are the power amplifier (due to CMOS transistors' inherent low current drive [15]), SAW filters, and crystal clock reference [16]. Strict spectral masks [17] and transmit power requirements dic-

3

tated by standard prevent further wide-spread CMOS integration of the three blocks [18].

In compact biomedical sensor nodes, system form factor needs to be in mm-range. As a result, there is not enough room for external filters, timing references, or power amplifiers. As a result, adopting such standards in this class of devices is not viable (Figure 1.1) despite all the benefits of using already-established standards.

- **Short-Range Links:** During recent years, integrated radios that are tailored for a specific application for a certain range have attracted a lot of attention [19]. Due to their near-field nature, these radios do not interfere with cellular, military, and industrial bands.

  One class of short-range radios are inductive links targeted for specific biomedical applications. However, most of the published work in biomedical applications use large receive antennas (larger than 1cm), eliminating the chance of using them in mm^3 biomedical implants [20]. The few previous works that use integrated antennas suffer from poor transmission range [21] or poor sensitivity [22]. The link proposed in [22], although being completely integrated and achieving 1m of range, lacks a downlink. Also, in the transmit side of the work mentioned in [22], the phase noise skirts of the two FSK tones have significant overlap, due to transmit inductor's low quality factor, which drastically degrades BER. In Chapter 2, we propose a dual-resonator architecture to mitigate this phase noise degradation in FSK transmitters.

1.1.3 Range Requirement

Biomedical implants push the envelope in medical research by providing either of the two tasks: sensing of vital signals [23] or stimulation of internal organs [24]. In both these classes of devices, achieving enough range in lossy body tissue is critical to system operation. A mm^3 through-tissue range of 1m is desired in most in-vivo measurements [25].

In context of range of active radios, it is also worthwhile to mention short-range radios designed to facilitate inter-later communication in 3D integrated circuits [26]. Despite being compact, fully integrated, and energy efficient, these near-field radios suffer from short

transmission range (typically sub-mm). As a result, this class of radios is incompatible with biomedical applications where a transmission range of 1m is desired (Figure 1.1).

In this thesis, the first-ever transceiver that can satisfy all the three requirements shown in Figure 1.1 is presented:

1. Achieves 1m of transmit and receive range

2. Can run off a compact 1-10 μAhr battery

3. mm^3-sized with no off-chip components

The transceiver that sits at the heart of a 3D stacked microsystem will be able to interface with other major low-power blocks designed for mm^2 sensor nodes to make a highly reconfigurable, compact microsystem. All system blocks are designed specifically for biomedical applications where carrier frequency and power density are limited by application requirements.

1.2   Inductive, Capacitive, and Far Field Links

There are three possible choices for the type of link we can use to talk to an implant inside tissue.

When transmitting signals across long distances, receiver will be receiving power from the radiated power originating from transmitter as shown in Figure 1.3. Far field approaches are widely used in wireless consumer products such as cell phones[13]. They benefit from availability of a wide variety of off-the-shelf integrated circuits. They can also enjoy low link loss due to the availability of high-gain antennas. Most importantly, unlike capacitive and inductive links, their received power reduces quadratically with distance which makes them superior to other link types when transmission distance is too long[27]. Despite all these benefits, they are not the best choice when transmitting through body tissue due to their excessive in-tissue loss and reflection at tissue boundary. Besides, as recent research has suggested[28], they have to operate at low-GHz range to achieve their optimum efficiency. However, antenna size at these frequencies has to be above a few centimeters to achieve
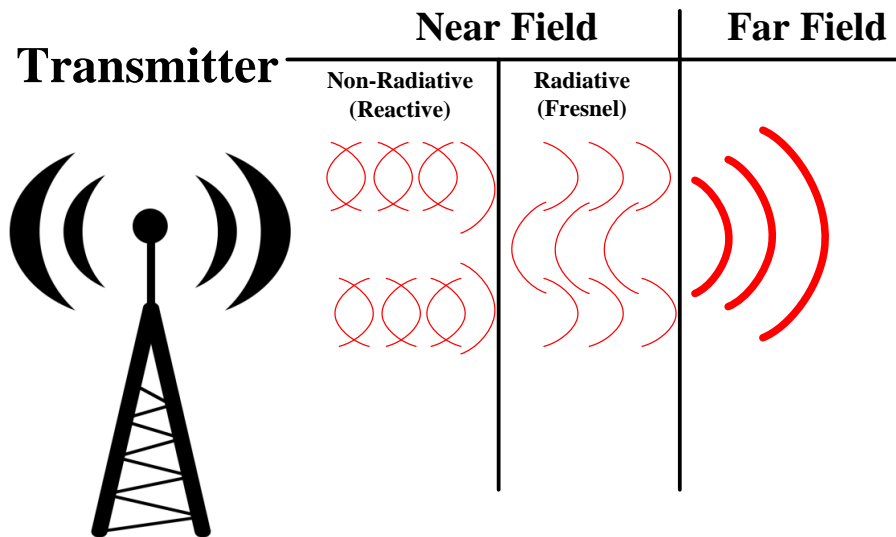
Figure 1.3: **Different wireless transmission regions.**

reasonable antenna gain, making them unattractive for highly compact systems. In most wireless biomedical links, transmission distance is in the order of few centimeters. This means that the receiver will be in the near-field region shown in Figure 1.3, thus, far field approaches are not as appealing for such applications.

Capacitive links provide an alternative choice[29]. Based on recent research, however, dielectric properties of different organic tissues vary drastically making it hard to design a link that can work for different implant depths and locations[30]. Besides, different body tissues have different non-negligible conductivities, that presents a major challenge. Also, some tissues like the muscle tissue have significant dielectric loss tangent which is going to make them inefficient at high frequencies.

Inductive links have been the dominant form for through-tissue data communication[31]. Human body does not show strong ferromagnetic behavior and its relative permeability is equal to 1 with a good approximation. Besides, magnetic loss tangent is not an important playing factor in organic materials. With the advent of modern 3D electromagnetic simulation tools, these nead-field mediums can be accurately modeled at design stage. Our design combines transmit inductor and oscillator inductor which eliminates the need for a power amplifier. Due to the inherent impedance match at resonance, there will be no need for bulky matching circuitry to drive the power amplifier either.
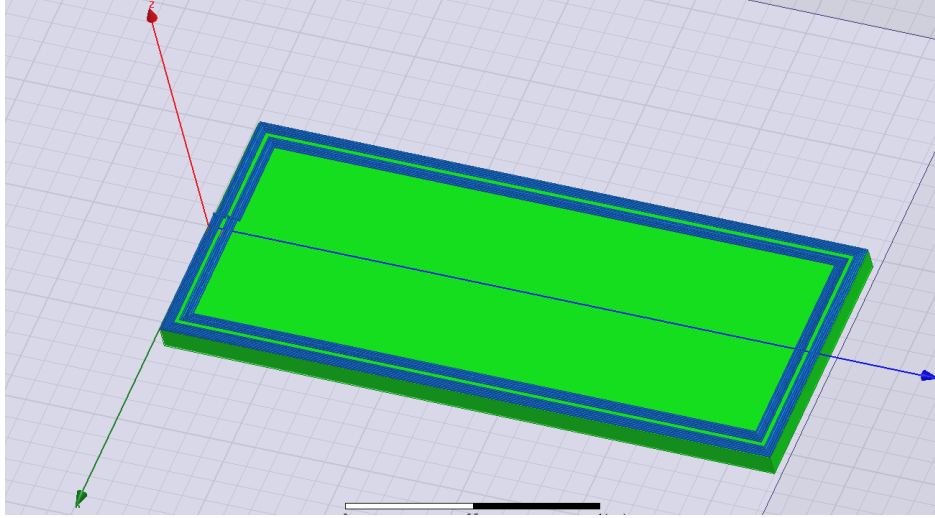
Figure 1.4: **HFSS Design of our on-chip inductor.**

In our link, we will be using on-chip inductors to couple to the external transceiver. This guarantees the highest level of integration with CMOS circuitry at the cost of reduced inductor quality factor. Since form factor is a more important criteria for biomedical microsystems, the lower Q-factor is acceptable. Figure 1.4 shows the 3D model of a $2mm \times 1mm$ inductor in 180nm CMOS process on silicon substrate. One advantage of having a big inductor is that CMOS circuits can be placed in the middle of the inductor to maximize efficient use of the available area.

Table 1.1 shows the characteristics of the mentioned inductor. It is able to achieve high inductance value while maintaining moderate quality factors. In an inductive link, the value of magnetic dipole moment plays a crucial role in determining total link loss:

$$m = NIS \tag{1.1}$$

where N is the number of inductor turns, I is the inductor current and S is the inductor area. By putting the CMOS circuitry inside the inductor, S will increase, enabling us to achieve higher magnetic dipole moment and, thus, higher transmission range. Table 1.1 clearly shows that, an optimized inductor can be made with high number of turns while maintaining reasonable Q-factors.

Table 1.1: **Characteristics of the on-chip Inductors.**

Parameter	Value
Dimentions: $d \times l$	$2.64mm \times 1.72mm$
Number of Turns: N	5
Turn Spacing: s	3μ
Inductance: L	$256nH$
Quality Factor at 915MHz:	4.9

1.3   Limitations of RF Circuits in Inductive Links

Due to small size, wireless transceivers uses in biomedical implants suffer from poor performance. As a result, their transmission distance will be compromised.

On the implant-to-external side (which we will refer to as uplink), transmitter has to drive the antenna, which is replaced with a transmit coil in our system. Transmitter performance is highly dependent on purity of its local frequency generator. Typical transmitters take advantage of a crystal oscillator to guarantee low phase noise [32]. In most cases a complex modulation scheme is used to ensure efficient use of frequency spectrum[33]. In biomedical implants, however, crystal oscillators are too big to fit in the system. The use of complex modulations is not an option either due to the high power overhead.

In order to tackle the phase noise limitation, we propose using an inherently dual-frequency structure along with frequency-shift-keying (FSK). In Chapter 2 a dual-resonator oscillator and power amplifier is introduced that can achieve high frequency separations without compromising phase noise.

Chapter 3 proposes a novel receiver architecture that can receive signals from the dual-resonator transmitter introduced in 2. It will be shown, through simulation and measurement, that such architecture is capable of receiving signals from two bands while rejecting other parts of the spectrum.

In Chapter 4, we propose a complete intraocular pressure microsystem. The transceiver used in that system uses the dual-passband architecture mentioned above. The transmitter was successfully implanted in animal tissue and achieved $10cm$ of transmission range.

On the external-to-implant side (which we will refer to as downlink), power and area are again limiting design factors. Analog RF front-ends are typically matched to a resistive antenna impedance at carrier frequency. This will ensure maximum power delivery to

the low-noise-amplifier (LNA). In inductive links, however, a receive coil replaces the resistive antenna as shown in Figure 1.5. In such a link, if we power-match the receiver input impedance, the loaded quality factor of the inductor will be half of the designed unloaded Q. This will reduce the voltage delivered to LNA gate by half, thus affecting our final achievable transmission range.

Apart from Q-degradation, there is another reason that makes power match approach unattractive for inductive receiver front-ends. Since common source CMOS LNA only presents imaginary input impedance, we have to use inductive degeneration to add a resistive component to the input impedance. For compact implantable inductive links, this translates to excessive area overhead which is undesired.

Apart from the mentioned reasons, there is another limitation that prevents us from lowering LNA power below a certain amount. Assume we would like to power-match the inductively-degenerated common-source LNA shown in Figure 1.5 without adding any extra capacitors and inductors (capacitors are undesired because they lower bandwidth and inductorss area overhead is also undesired). The source inductor L_s will be in series with the receiver inductor L_{int}. We would like to minimize the number of passives and use the MOS transistors's C_{gs} capacitor to resonate out $L_s + L_{int}$. The resistive component of input impedance is:

$$Re\{Zin\} = g_m L_s / C_{gs} \tag{1.2}$$

On the other hand, we would like C_{gs} capacitor to resonate out $L_s + L_{int}$, so:

$$f_0 = \frac{1}{\sqrt{2\pi(L_{int} + L_s)C_{gs}}} \tag{1.3}$$

Combining 1.2 and 1.3 and assuming a 50Ω match at $f_0 = 915MHz$ limits our transistor bias current to $I_{DS} > 1mA$ as shown in Figure 1.6. This plot assumes a $w = 512\mu m$ device in 180nm RF CMOS process.

In Chapter 4, we proposed an ultra-low-power passive receiver for the downlink of the system. The passive receiver achieved $4mm$ of range with a 1-Watt external transmitter. The IOPM can be wirelessly programmed through its downlink which simplifies its application in clinical environment.
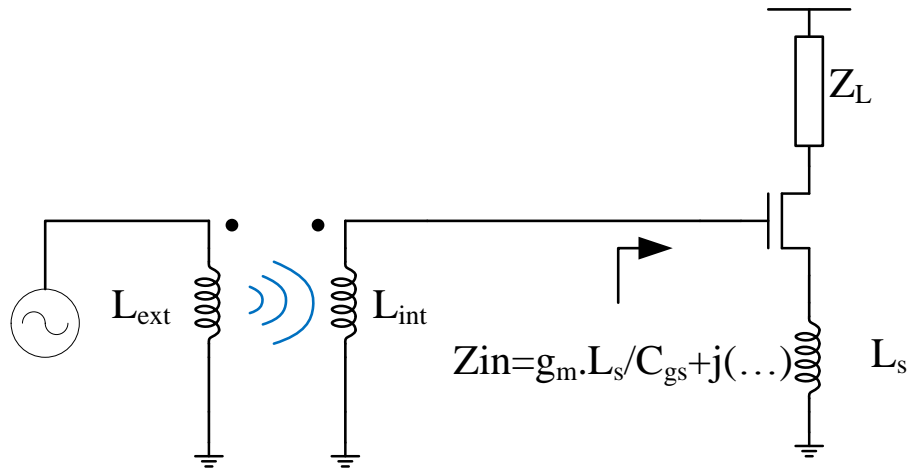
(a)
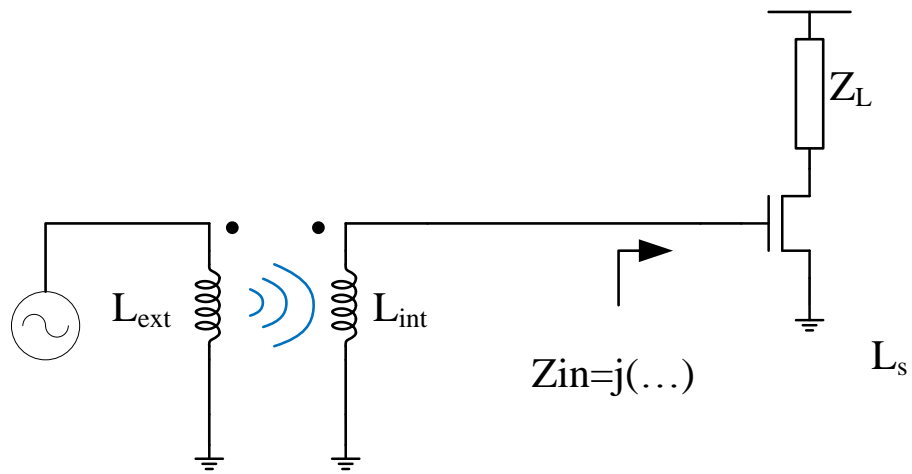
(b)

Figure 1.5: **Inductive link front-end configurations.** (a) Front-end designed for maximum power delivery (b) Front-end designed for maximum voltage
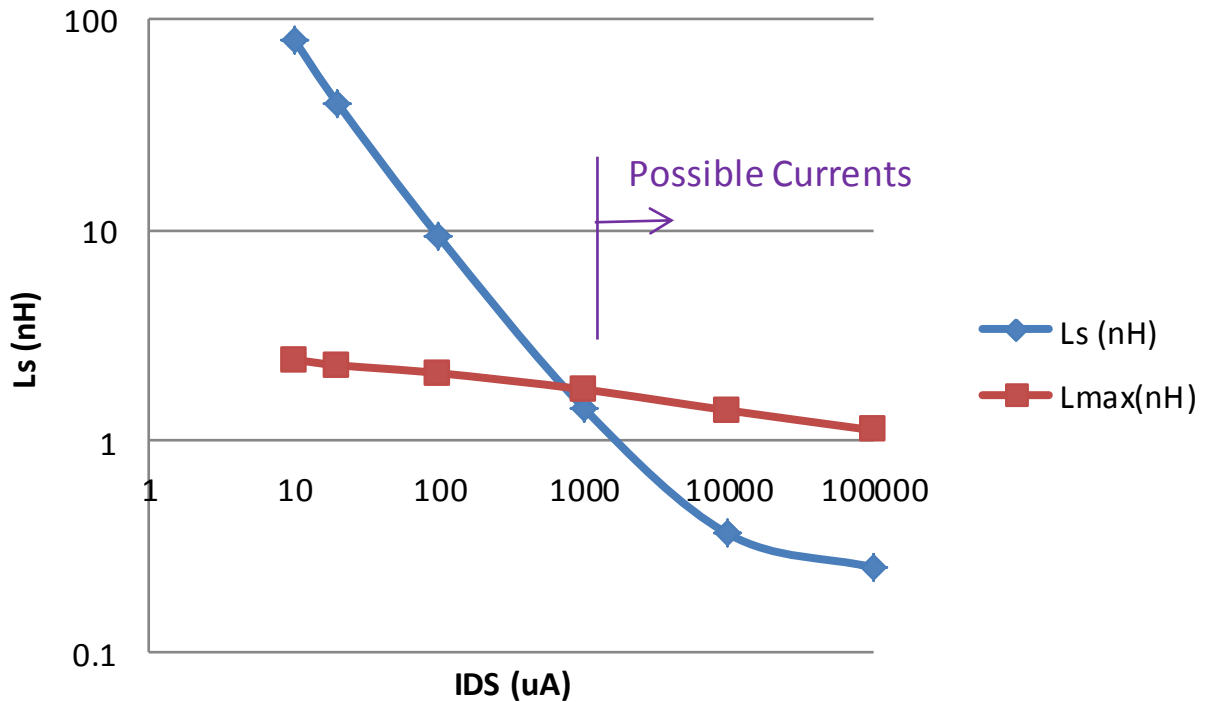
Figure 1.6: **Design space for power match at 915MHz in 180nm CMOS process node.**

In order to increase the range of our downlink, the passive receiver can be replaced with an active RF front-end with higher sensitivity. Chapter 5 presents an active receiver front-end that can receive data from a 2W external unit positioned 1m away. The front-end uses a novel protocol to push power consumption to external side, thus relaxing the synchronization constraints on the chip side. It also uses a duty-cycling scheme to lower the peak power drawn from its thin-film battery to 19.9 μW. The receiver was fabricated and successfully tested in 180nm CMOS.

Chapter 6 summarizes the important advances in the inductive short-range links made possible through the techniques described in this thesis. It also outlines possible future work in this field.

1.4   Tissue Heating

Out proposed link will consist of an implanted device buried under the skin with a 1-Watt external transmitter located 5 cm away. Due to the high level of transmit power, it is

Table 1.2: **FCC compliance of the proposed link.**

Parameter	Allowed by FCC	Compliance
Specific Absorption Rate(SAR)	$1.6W/Kg$	Yes at $d > 1.2mm$
Power Density (Local)	$0.28mW/cm^2$	Yes at $d > 10mm$
Power Density (Total Body)	8	Yes

necessary to check the compliance of such link with electromagnetic exposure standards.

Although effects of high levels of electromagnetic exposure on human body are still not completely known, Federal Communications Commission (FCC) has put limits on radiation levels. Even though these limits were put with hand-held electronic devices in mind, any biomedical device that talks to an external wand should still follow the guidelines to minimize the the risk of tissue damage.

The first part of FCC regulations, involves the Specific Absorption Rate (SAR) within body. SAR can be calculated from the electric field within tissue as:

$$SAR = \int \frac{\sigma(r)|E(r)|^2}{\rho(r)} dr \tag{1.4}$$

where σ is the sample electrical conductivity, E is the RMS electric field, and ρ is the sample density. In US, FCC requires that devices have a SAR level at or below 1.6 watts per kilogram taken over a volume of 1 gram of tissue. Figure 1.7 shows the simulated skin tissue with the external transmitter coil. The simulation results are summarized in Table 1.2.

The second and third FCC regulation deal with local and total electromagnetic power density in body tissue. FCC limitations as well as out device compliance for these two are also listed in Table 1.2.

1.5   Link Optimization

In order to maximize the amount of voltage delivered to the receiver coil, we need to quantify the amount of voltage delivered to first gain stage on the receive side. Figure 1.8 shows the link model which consists of two inductors L_1 and L_2 with quality factors Q_1 and Q_2. Power is delivered to L_1 from the transmitter source Pin which is power-matched to the series resistance of L_1 i.e. R_{s1}. LNA input capacitance is designed such that it resonates
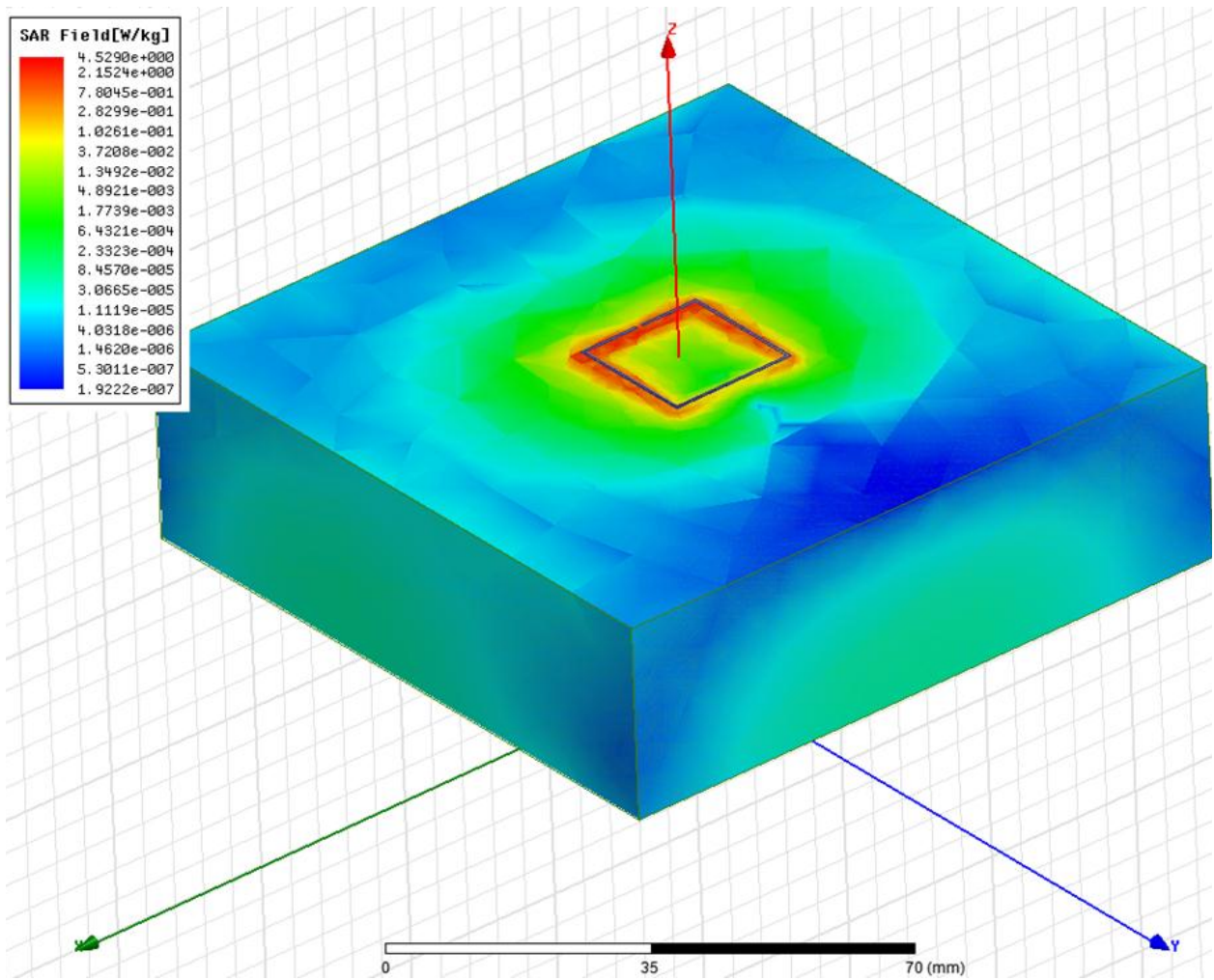
Figure 1.7: **Surface absorption rate in body tissue for a 1W inductive transmitter placed 1mm away .**
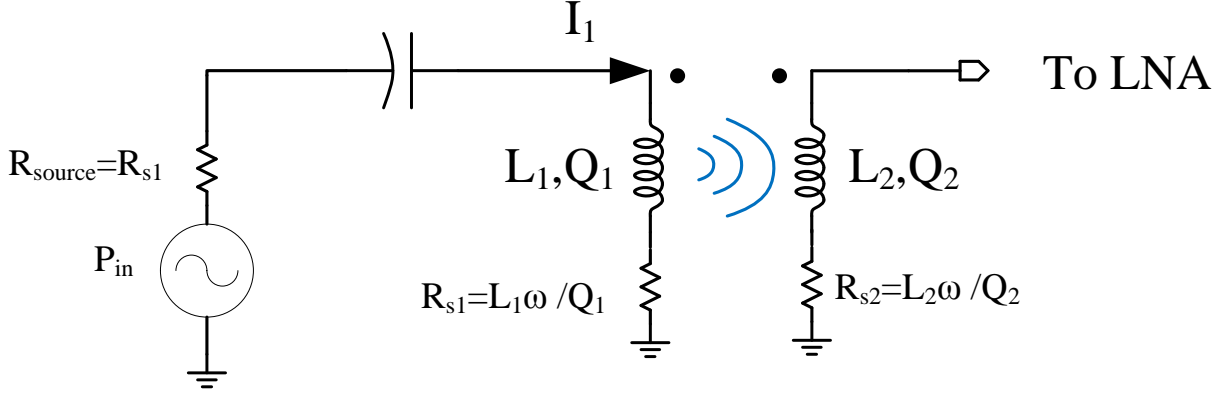
Figure 1.8: **Circuit model for an inductive link.**

out L_2 at the center frequency.

On the transmit side, assuming a matched load, we have:

$$P_{in} = \frac{V_{in}^2}{2R_{s1}} \tag{1.5}$$

On the receive side, assuming resonance at the center frequency ω_0, the voltage at LNA gate would be

$$V_G = Q_2 M \frac{dI_{1(j\omega)}}{dt} \tag{1.6}$$

$$= Q_2 k\sqrt{L_1 L_2}\frac{d[\frac{Vin_{(j\omega)}}{\frac{L\omega}{Q_1}}]}{dt} \tag{1.7}$$

$$= Q_2 k\sqrt{L_1 L_2}\omega\frac{Q_1 V_i n}{L_1 \omega} \tag{1.8}$$

plugging 1.9 in 1.8 gives us received voltage in terms of transmitter power:

$$V_G = kQ_2\sqrt{2Q_1 L_2 P_{in}\omega} \tag{1.9}$$

The above equation can be used to maximize the receive voltage. By simulating the coupling factor of the two inductors using HFSS, we can guarantee that the received voltage will be above the sensitivity of our receiver. The external inductor size was picked to be 10 times bigger than the integrated receive antenna to maximize k. Note that the external coil cannot be arbitrarily big because the self-resonant frequency for cm-size coils are below

14

1GHz. Also, note that received voltage will only increase by a factor of $\sqrt{2}$ when Q_2 is doubled. This justifies our choice to make the receive coil as large as possible and fit all other circuitry inside the inductor at the cost of slightly reducing quality factor Q_2.

1.6   Synchronization

Data transmission is not possible without synchronizing the receiver and transmitter to each other. The synchronization issue becomes more pronounced in sensor nodes where peak power is highly limited. Due to the small size of battery in such systems, battery is unable to continuously power the active receiver which burns close to 1mA of current. In order to solve this issue we propose adding 10nF of decoupling capacitor to power the receiver during data reception and turn off the power-hungry transceiver and receiver to recharge these capacitors between data packets.

On the sensor to external side, our on-chip transmitter turns on for a short period to transmit tones at either 433MHz or 915MHz ISM frequencies and shuts off. The external unit, which is always listening, detects these tones and interprets them as 1's and 0's. This scheme was successfully implemented and tested in the intraocular pressure sensing microsystem in Chapter 4.

On the external to sensor side, since the on-chip receiver can only monitor its input for a short window, a new protocol is proposed to shift power consumption to the external unit side. In this scheme, external unit repeatedly sends the same data, which gives the receiver freedom to wake up and capture data whenever it likes. As a result, jitter requirement on the chip side is drastically relaxed. A transceiver that successfully receives data is presented in Chapter 5.

CHAPTER 2

Analysis and Design of Stable Dual-Resonator Oscillators

2.1   Motivation and Related Work

Dual band communication systems have attracted a lot of attention with the introduction of new technologies in higher frequency bands. Wireless LAN, for example, has used the 2.4GHz band in its earlier versions, but switched to 5GHz to achieve higher bandwidth[34].

In order to realize a dual band transceiver, the oscillator must be able to synthesize both frequencies. Conventional single-tank oscillators have limited tuning range that cannot cover two different bands. In addition, increasing the tuning range worsens phase noise[35]. Using a dual-resonating tank can enable dual-band operation without sacrificing system performance. The schematic for such an oscillator with a dual-resonating tank is shown in Figure 2.1. The two tanks are tuned to two different frequencies f_1 and f_2 which can be arbitrarily chosen, making it possible to realize an oscillator with inherent doubl-frequency capabilities.

Switching from a single-resonance tank to a dual-resonance tank changes the system dynamics. The question that arises here is whether the oscillator will oscillator at the first, second, or both of the frequencies. In [36], the authors derived nonlinear models for the oscillator and concluded that the system can only oscillate at one of the two frequencies, which are both stable. They suggested that it is possible to switch between these two states
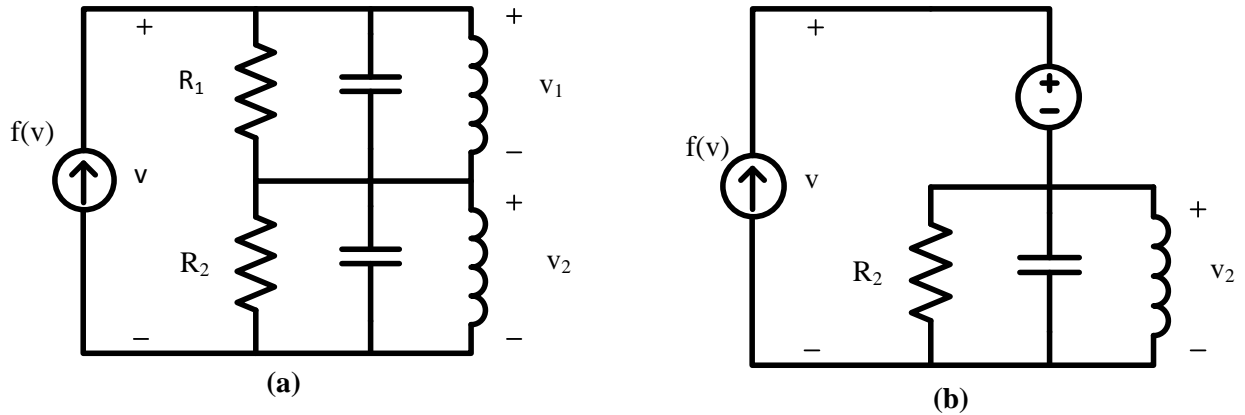
Figure 2.1: **Equivalent circuits for an oscillator with dual-resonating tank.** (a) The original schematic without simplifications. (b) Simplified schematic to model the transient circuit behavior while the first tank oscillates with approximately constant amplitude.

by shorting either tank , allowing oscillations to form in the other tank. They proposed that the system will remain oscillating at the same frequency when the switch is released. This chapter shows through measurement results that conditions must be satisfied for this to occur. In other words, either of the frequencies can go unstable if not properly designed. Two 0.18um CMOS oscillators were fabricated to validate this concept. Measurement results show instability in one of the chips at the designed frequency.

2.2   Model Derivation

In order to form oscillations at ω_1, the second tank is shorted. Then, the switch just used to short the second tank is opened to avoid the excessive phase noise it adds to the tank. The tank is expected to remain oscillating at ω_1. This is referred to as stable oscillations at that frequency. The authors of [36] comprehensively studied the state space of the system and derived the phase portrait for the system. However, the problem was oversimplified since the effect of tanks on each other during transitions was neglected. As shown in Figure 2.2, oscillations at the first frequency can be unstable in contrast to what was derived in [36]. Note also that the oscillation amplitude across the tank that was oscillating before the switch is opened is nearly constant until significant oscillations are formed in the other tank. Let us refer to the first tank as the aggressor and the second one as the victim. In other words, an

17
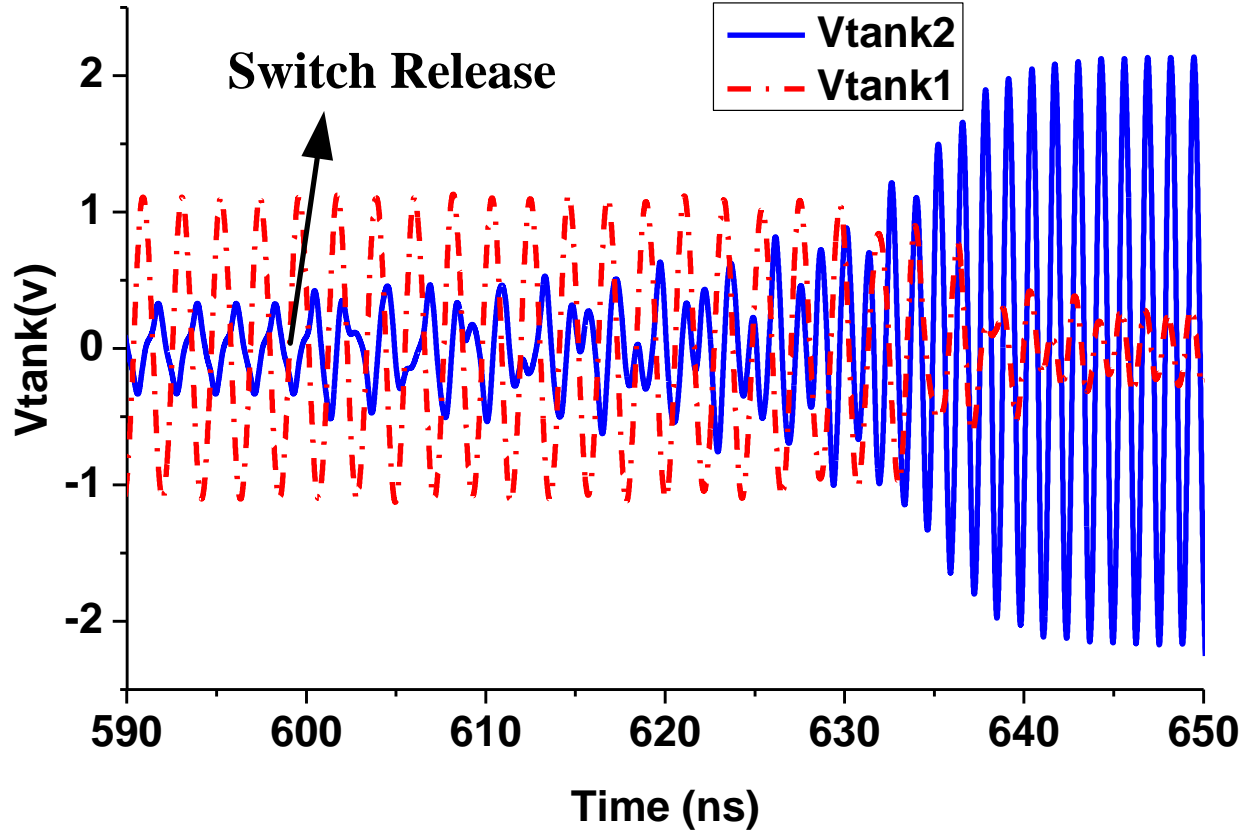
Figure 2.2: **Simulated voltages of a dual-resonator tank after opening the switch that shorts the second tank. Oscillations can build up at the second tanks frequency (f_2), resulting in loss of the previous state of oscillating at f_1.**

unwanted instability occurs when the victim manages to form oscillations with the aggressor present. To simplify the problem, we can assume that until significant oscillations are formed in the victim tank, the aggressor acts as a sinusoidal source with constant amplitude A_1. The simplified schematic is shown Figure 2.1 Using Kirchhoff's Current Law(KVL):

$$f_{(v)} = i_R + i_C + i_L \tag{2.1}$$

$$= \frac{v_2}{R_2} + C_2\dot{v}_2 + \frac{1}{L_2}\int v_2 dt \tag{2.2}$$

Differentiation yields:

$$f'_{(v)}\dot{v} = C_2\ddot{v}_2 + \frac{\dot{v}_2}{R_2} + \frac{1}{L_2}v_2 \tag{2.3}$$

18

Modeling the negative impedance as

$$f_{(v)} = k_1 v + k_3 v^3 \tag{2.4}$$

results in a form similar to the well-known van der Pol [37] equation:

$$(k_1 + 3k_3 + v^2)\dot{v} = C_2 \ddot{v}_2 + \frac{\dot{v}_2}{R_2} + \frac{1}{L_2} v_2 \tag{2.5}$$

Note that k_1 is equal to the absolute value of the negative g_m presented to the tank while k_3 models the voltage-limited nature of the circuit. Applying Kirchhoff's Voltage Law (KVL):

$$v = v_2 + A_1 \sin(\omega t) \tag{2.6}$$

Thus, we can re-write 2.5 as:

$$(k_1 + 3k_3(A_1 \sin(\omega_1 t) + v_2)^2)(A_1 \omega_1 \cos(\omega_1 t) + \dot{v}_2) = C_2 \ddot{v}_2 + \frac{\dot{v}_2}{R_2} + \frac{1}{L_2} v_2 \tag{2.7}$$

To approximate the behavior of the victim tank oscillations in presence of the aggressor, we expand it and its derivative as suggested in [38]:

$$v_2 = A_2 \sin(\omega_2 t) \tag{2.8}$$

$$\dot{v}_2 = A_2 \cos(\omega_2 t) \tag{2.9}$$

Differentiation yields:

$$f'_{(v)}\dot{v} = C_2 \ddot{v}_2 + \frac{v \dot{+} 2}{R_2} + \frac{1}{L_2} v_2 \tag{2.10}$$

The differential equation can be expanded to the first order to the form: Thus, we can re-write 2.5 as:

$$C_2 v_2 + \frac{1}{L_2} v_2 = (k_1 + \frac{3}{4} k_3 A_2^2 - \frac{1}{R_2}) A_2 \omega_2 \cos(\omega_2 t) \tag{2.11}$$

The condition to avoid self-excitation [38] is given by:

$$\overline{\lambda_{(0)}} = \frac{1}{R_2} - \frac{3}{2} k_3 A_1^2 - k_1 > 0 \tag{2.12}$$

19

Assuming transistor transconductances, k_1 and k_3 are independent of frequency, we can further simplify the condition. We can derive the value of A_1 as the limit cycle amplitude in van der Pol equation [39] at the first frequency:

$$\frac{3}{2}k_3 A_1^2 = \frac{2}{R_{1(\omega_1)}} - \frac{2}{k_1} \tag{2.13}$$

Plugging 2.13 into 2.12 results in:

$$\frac{2}{R_{1(\omega_1)}} - \frac{1}{R_{2(\omega_2)}}g_m \tag{2.14}$$

Hence, as long as the two frequencies are not too far apart to have different g_m values, 2.14 describes the necessary condition for stable oscillations at the first frequency, ω_1. Similarly, in order to have stable oscillations at ω_2 the following condition must hold:

$$\frac{2}{R_{2(\omega_2)}} - \frac{1}{R_{1(\omega_1}} > g_m \tag{2.15}$$

2.3 Design and Measurement Results

To verify the validity of the derived model, two chips with identical inductors were designed and fabricated in the same 0.18um CMOS process. Chip micrographs of both chips are shown in Figure 2.3. The goal of the design was a fully integrated inductive coupling transmitter using the coils as transmission coils in our inductive link. By integrating the oscillator and power amplifier (PA), the stringent area constraint imposed by the implantable sensor application was met. The designed transmitter was used as a part of the intraocular pressure sensor presented in [40]. The dual-resonator architecture enables us to implement FSK modulation with two frequencies located far from each other, thus relaxing the constraints on phase noise and resulting in better BER.

As suggested by 2.14, one way to avoid instability is to reduce the absolute value of the negative gm presented to the tank. In other words, oscillators designed in the voltage-limited regime are more likely to go unstable due to their excessive g_m. Note that in the transmitter designed for the intraocular pressure sensor [7], we preferred high gm values so that more
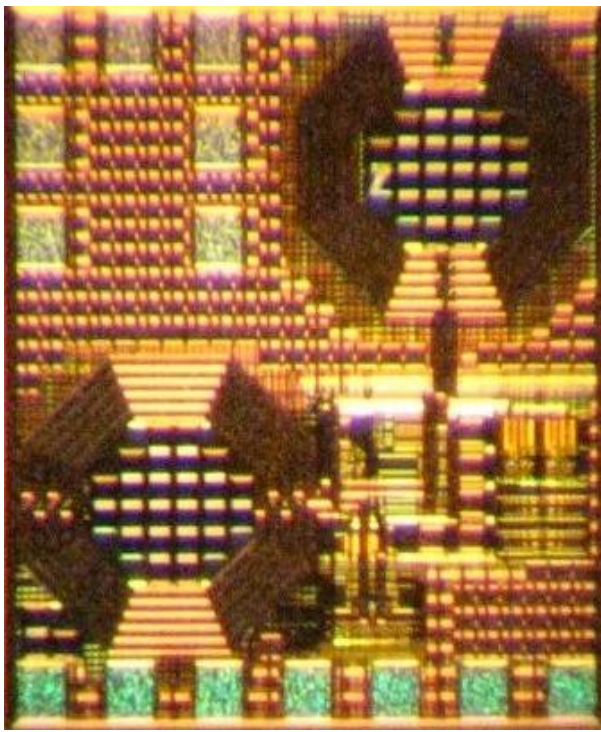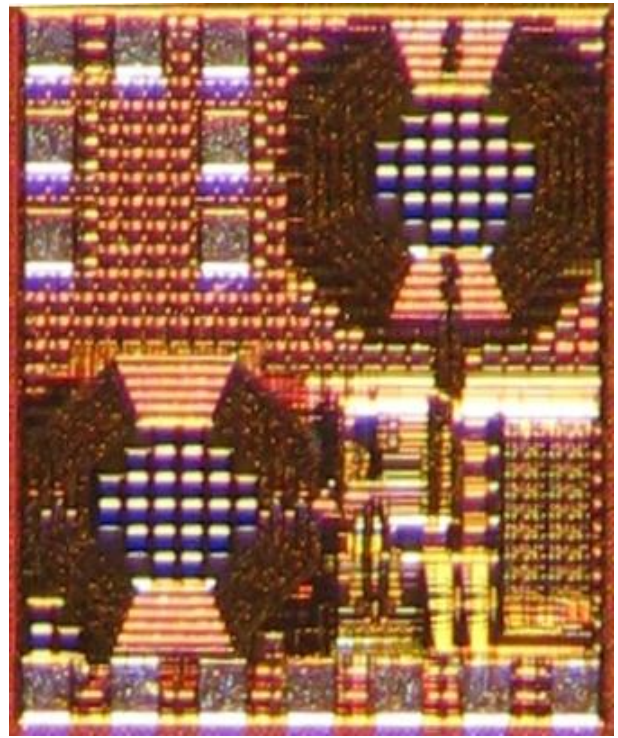
(a)　　　　　**(b)**

Figure 2.3: **Chip micro-graphs of the two fabricated CMOS chips. The transmitter was used in the radio layer of an integred intraocular pressure sensor microsystem[7]** (a)The unstable oscillator (b) The version with modified frequency separation to overcome oscillator instability.
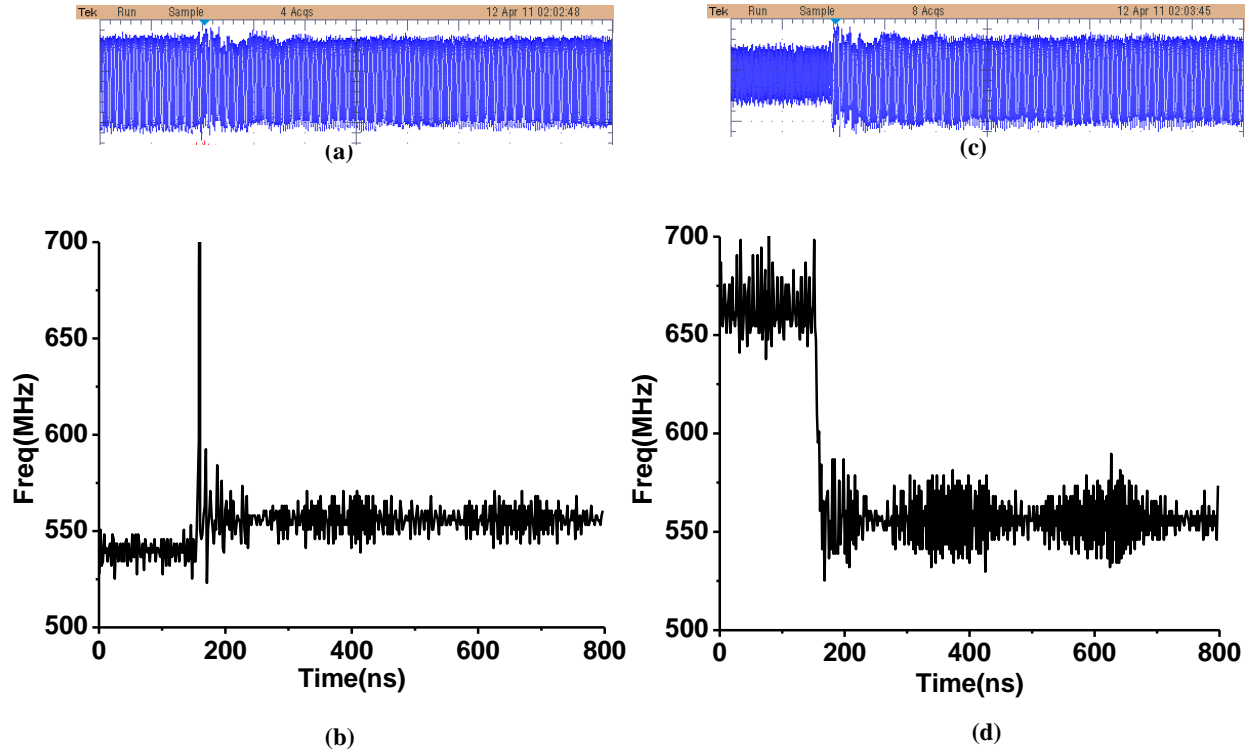
Figure 2.4: **Unstable oscillator results** (a,b) Normalized tank voltage and frequency upon release of the switch that was shorting the second tank. The tank keeps oscillating at the original frequency. (c,d) The same results for the case when the switch shorting the first tank is released. This time, the oscillator starts to oscillate at the new frequency.

power is delivered to the coil and higher transmission distances can be achieved. In this way, there is a trade-off between stability and the amount of power delivered to the coils.

Another approach to achieve stability at ω_1 is to decrease R_1 in 2.14. However, decreasing R_1 is equivalent to reducing the quality factor of the tank, resulting in lower transmission range and higher phase noise in our inductive link, which is not acceptable.

Figure 2.4 shows measurement results for a dual-resonator oscillator with $f_1 = 540MHz$ and $f_2 = 660MHz$ that was intentionally designed to be unstable at f_2 (Figure 2.3). As shown in Figure 2.4, oscillations at f_1 are stable as the tank continues to oscillate at the same frequency upon releasing the switch shoring the second tank. This is not the case for oscillations at f_2, as seen in Figure 2.4 The oscillation frequency changes after the switch shorting the first tank is opened because the g_m value is high enough to suppress the pre-existing state.

Figure 2.5 shows measurement waveforms for the second version of the oscillator using
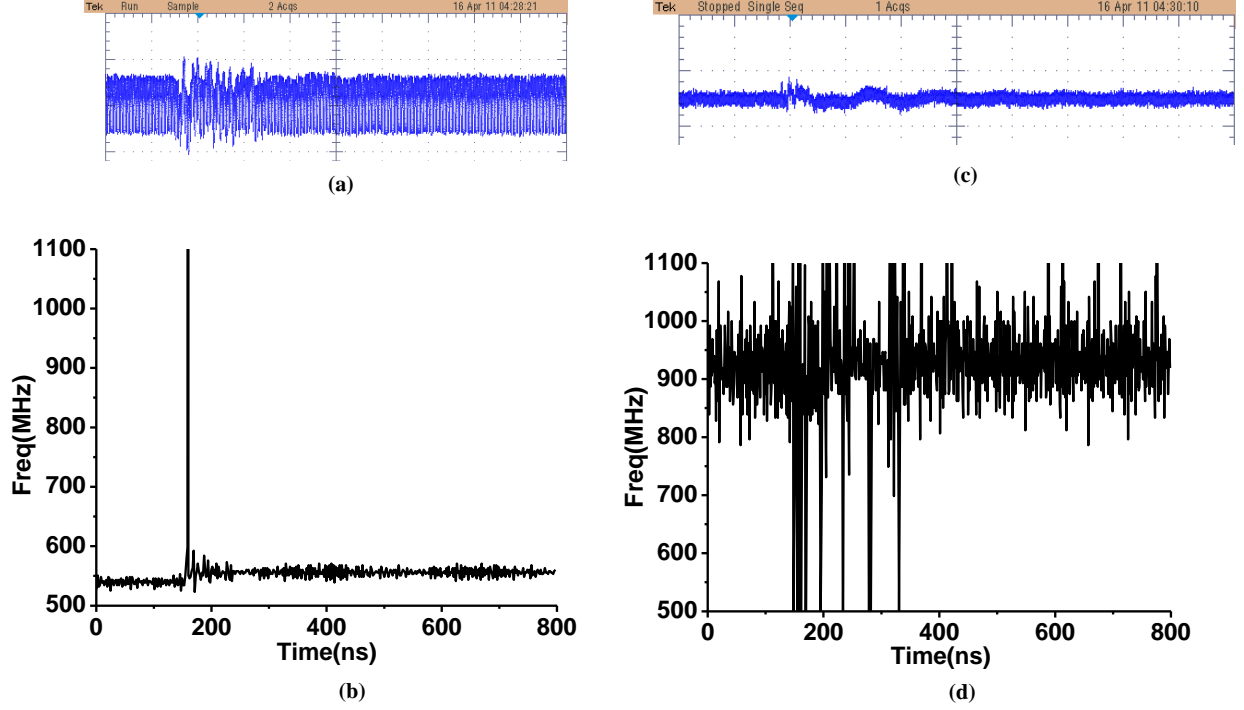
Figure 2.5: **Stable oscillator results** (a,b) Normalized tank voltage and frequency upon release of the switch that was shorting the second tank. (c,d) The same results for the case when the switch shorting the first tank is released. In both cases, the tank keeps oscillating at the original frequency.

identically designed inductors and different frequency separation. This time, the transmitter can hold its state after either of the switches shorting the tanks is opened, thereby achieving fully-stable operation.

Let us examine the validity of the model by checking the stability condition in our two chips at the higher frequencies. Since the frequencies are far apart, we cannot use the simplified equations. Re-writing 2.12 for the second frequency gives us the stability criteria for ω_2.

$$\overline{\lambda_{(0)}} = \frac{1}{R_2} - \frac{3}{2}k_3 A_1^2 - k_1 = \begin{cases} -0.79\frac{1}{\Omega} < 0 \rightarrow unstable & \text{First Chip} \\ +0.74\frac{1}{\Omega} > 0 \rightarrow stable & \text{Second Chip} \end{cases} \quad (2.16)$$

where we have used simulation results to extract the required parameters at the two upper frequencies. Note that the stability condition is only satisfied for the second chip.

23

This is in agreement with our measurements in Fig 4.d and Fig 5.d.

2.4 Summary

As was shown through silicon and simulation results, designing oscillators with dual-resonator tanks can be challenging due to the possibility of state loss that was previously unknown. This work derived a model that describes the conditions that must be satisfied to guarantee a robust design. We showed that the choice of the negative transconductance, tank quality factors, and frequency separation impact the ability of the system to holds its state.

CHAPTER 3

A Novel Dual-Passband Receiver Architecture for Dual-Band Systems

3.1 Motivation

During recent years, wireless standards have been developed in previously unused frequency bands. WLAN, for example, used the 2 .4GHz band in its earlier versions then switched to 5GHz for improved speed [41]. Obviously, due to backward-compatibility issues, a system that can operate at both bands is desired. There has been significant interest in developing an RF front end that can cover different bands [42]. Figure 3.1 shows the two possible choices for a dual-band receiver front end. In the first approach all system components are duplicated. This approach is neither cost-effective nor area-efficient. A smarter approach designs the elements such that they can operate at both frequencies of interest. This method, shown in Figure 3.1, eliminates the need to duplicate the power-hungry RF components and also saves space by removing bulky passives.

Few design methodologies have been proposed in literature for designing the dual-passband matching networks [43, 44]. In [43] a complex design methodology for design of microstrip bandpass filters is presented that requires characterizing the technology by building a 2-dimentional design space. However, there is a possibility that the optimal point does not fall in the valid design space. Reference [44] proposed introducing three zeros to the transfer function by adding three stubs. However, this results in a 5-way microstrip junction that is
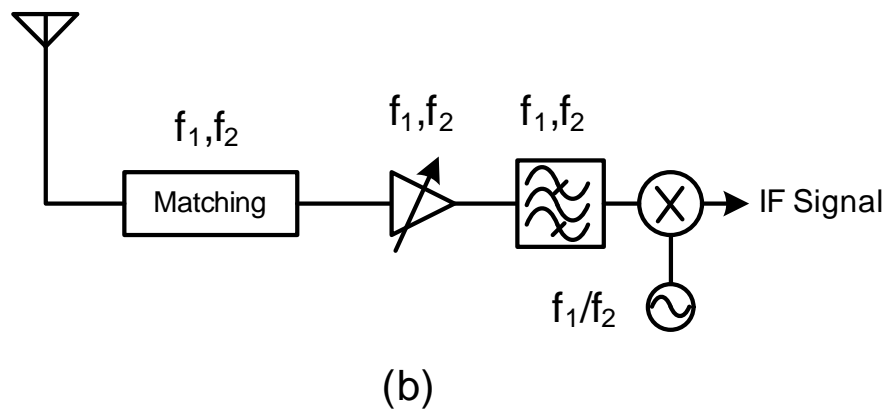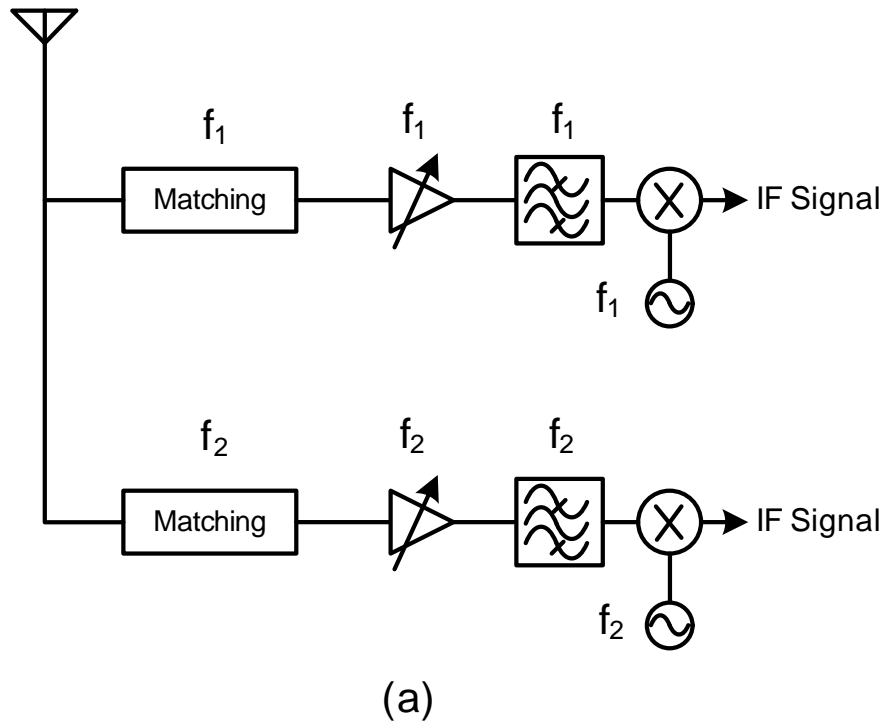
Figure 3.1: **Different analog front-ends.** (a) Conventional dual-band receiver front-end. (b) Inherently dual-band receiver front-end.

difficult to model and thus cannot be optimized easily. In addition, the aforementioned approaches assume a 50Ω effective load resistance at the desired frequencies. However, in many applications such as inductively-powered biomedical implants the antenna is replaced with an inductor that is resonating in an LC structure [45]. Thus, the antenna input impedance will be a large real number. Conventionally, bulky transformers or quarter-wave transformers have been used in these cases. The proposed dual-passband network has the advantage that it can match to arbitrarily large impedances without additional circuits.

In this chapter, we introduced a matching network for dual-band systems shown in Figure 3.2. The approach proposes a novel method to match high real-valued impedance to standard LNA input impedance of 50Ω.

3.2 Qualitative Description of the Approach

Assume two LC resonators are connected in series as shown in Figure 3.2. Our goal is to design a matching network that can provide 50 real impedance at both resonance frequencies.

Figure 3.2 also depicts the absolute value of the dual-resonator tank impedance [46] where Rs is the series resistance of the tank inductors and Q is the quality factor. For a typical microstrip coil with a quality factor of approximately 100 and series resistance of 0.1-1, the impedance seen will be more than 1k. Thus, designing a matching network becomes very challenging. Note that we expect the final circuit to be very narrowband according to the Bode-Fano criterion [47].

In order to tackle the high ratio of load over source impedance, consider the well-known Chebyshev equal-ripple filter illustrated in Figure 3.3. It is well known that for an even number of stages, N, the load impedance required to satisfy matching condition becomes larger than the source impedance [48]. We define this ratio as:

$$\alpha = \frac{R_L}{R_S} \tag{3.1}$$

However, note that α increases with the amount of ripple in the desired filter. Figure 3.3 shows this dependency. Increased ripple can be considered as the formation of better "stop-bands".
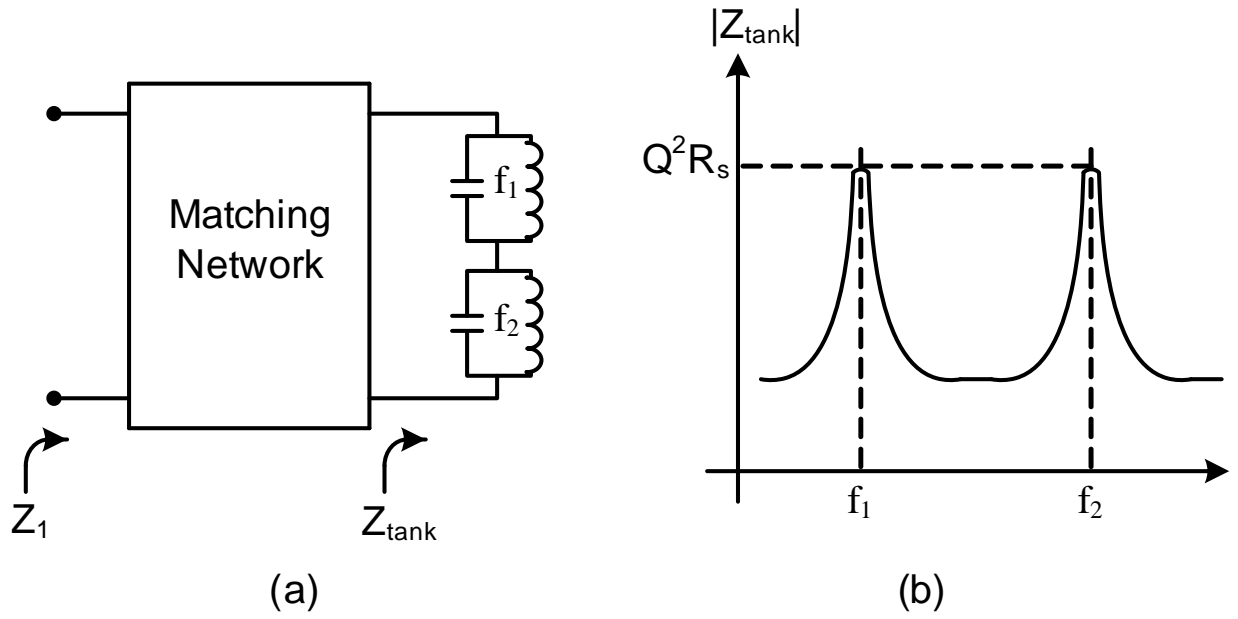
Figure 3.2: **Circuit Models for dual-resonator tank.** a) Matching network for a dual-resonator tank. (b) Impedance of a dual-resonator tank.

To this point we have built a high-ripple low-pass filter. If we now apply a lowpass-to-bandpass transformation on the filter, a bandpass filter with multiple passbands will be formed as shown in Figure 3.1. This way, the high α challenge has been overcome while simultaneously achieving a multiple-passband response.
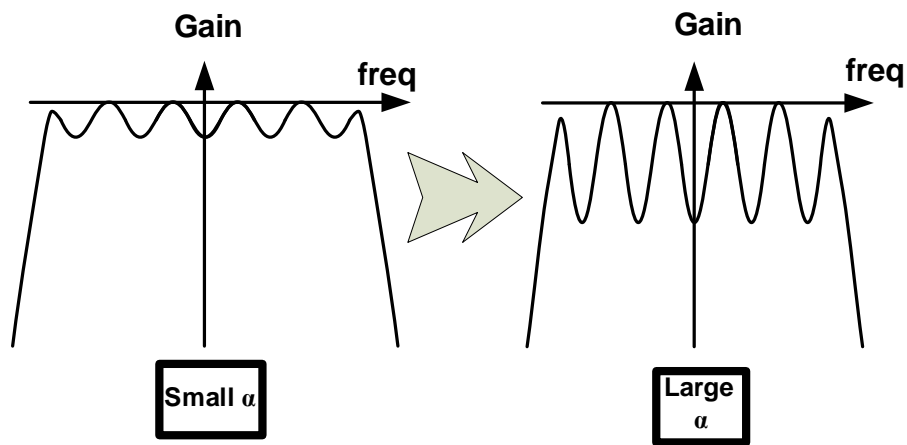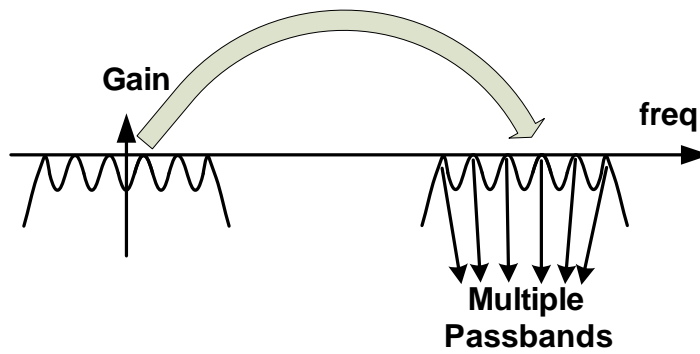
Figure 3.3: **Transformation of a Chebyshev filter.** (a) For a Chebyshev filter, ripple increases as we increase α. (b) Transforming a high-ripple low-pass Chebyshev filter to bandpass filter enables the design of filters with multiple passbands.

3.3 Model Derivation

Based on the described approach we can determine appropriate L and C values that provide matching for a given , 1, and 2. Specifically, the input impedance and reflection coefficient of the second order Chebyshev filter can be derived as

$$Z_{in} = j\omega L + \frac{R(1 - j\omega RC)}{1 + \omega^2 R^2 C^2} \tag{3.2}$$

$$\Gamma = \frac{Z_{in} - 1}{Z_{in} + 1} \tag{3.3}$$

Here R is the load resistance normalized to Rs=50Ω and other impedance values are also normalized to the same value.

The power loss ratio can be written as

$$P_{LR} = \frac{1}{1 - \Gamma^2} \tag{3.4}$$

$$= 1 + \frac{1}{4R}[(1 - R)^2 + R^2 C^2 + L^2 - 2LCR^2)\omega^2 + L^2 C^2 R^2 \omega^4] \tag{3.5}$$

We need to equate that with Chebyshev polynomial of 2nd order:

$$P_{LR} = 1 + k^2 T_{2(\omega)}^2 = 1 + k^2(4\omega^4 - 4\omega^2 + 1) \tag{3.6}$$

This results in:

$$k^2 = \frac{(1 - R)^2}{4R} \tag{3.7}$$

$$4k^2 = \frac{1}{4R}L^2 R^2 C^2 \tag{3.8}$$

$$4k^2 = \frac{1}{4R}(R^2 C^2 + L^2 - 2LCR^2) \tag{3.9}$$

Note that the amount of ripple required, k, is only dependent on R. After solving the first equation for k, L and C will be determined using the two other equations. L and C correspond to the values for the low-pass equivalent of the filter. As a result, we must perform a low-pass to band-pass transformation. Let us choose the transformed filter to be
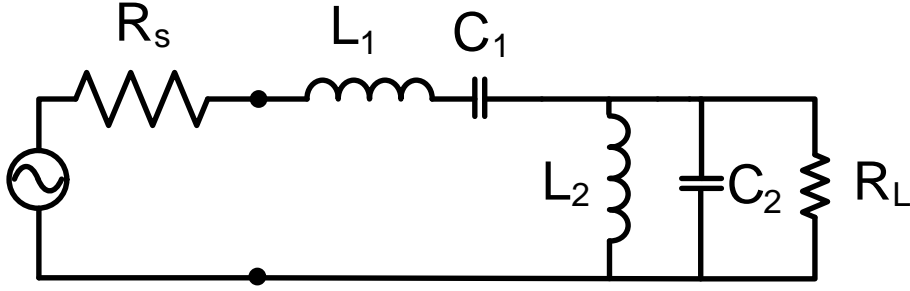
Figure 3.4: **The final matching circuit consisting of two inductors and two capacitors.**

centered at the geometric mean of the two desired frequencies with bandwidth $2(\omega_2 - \omega_1)$. Therefore, the values for the final circuit elements shown in Figure 3.4 are:

$$L_1 = \frac{LZ_0}{\omega_0 \Delta} \tag{3.10}$$

$$C_1 = \frac{\Delta}{\omega_0 L Z_0} \tag{3.11}$$

$$L_2 = \frac{\Delta Z_0}{\omega_0 C} \tag{3.12}$$

$$C_c = \frac{C}{\omega_0 \Delta Z_0} \tag{3.13}$$

where:

$$\Delta = \frac{\omega_2 - \omega_1}{\omega_0} \tag{3.14}$$

$$\omega_0 = \sqrt{\omega_2 \omega_1} \tag{3.15}$$

3.4 Simulation and Measurement Results

Based on the proposed method, a dual-passband filter was designed to match a dual-resonator load to 50. Figure 3.5 shows a dual-resonator tank and its matching network. The tank inductors are realized using PCB traces as is common in inductive power transfer schemes [28]. Figure 3.6 shows the simulated impedance of the tank using the Method of

31

Figure 3.5: **The dual-resonator tank and its matching network. The two loops on the right act as coils for tanks.**

(a)

(b)
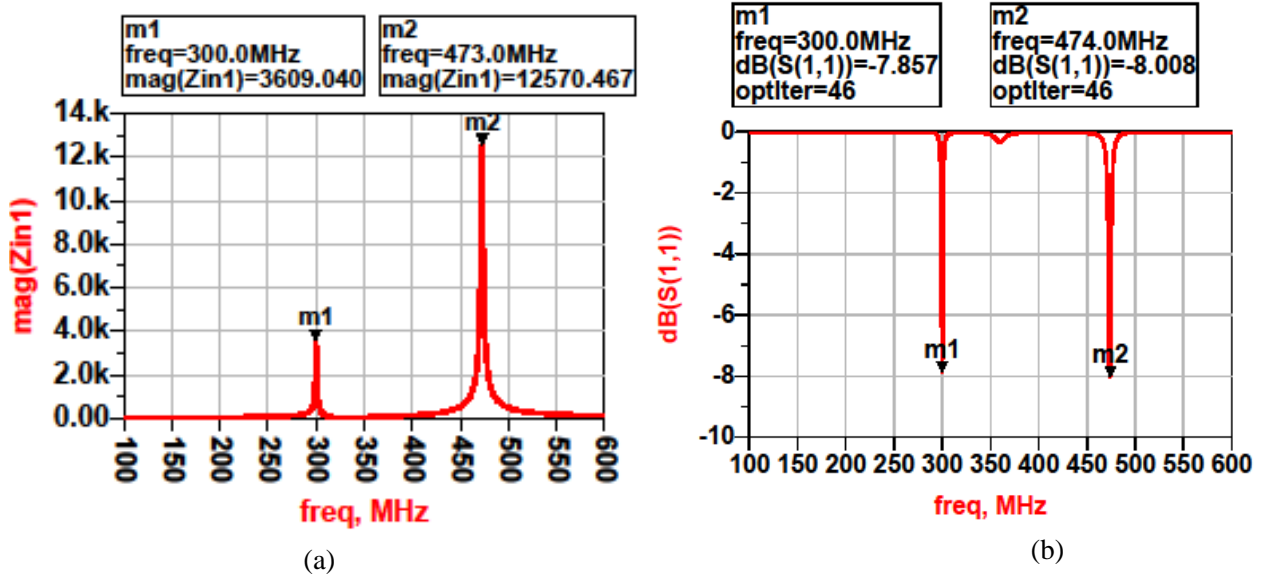
Figure 3.6: **Matching network simulation results.** (a) EM-simulated impedance of the dual-resonator tank. (b) Simulated reflection coefficient of the final circuit.

Moments. Thus, the load impedance at the resonance frequency is

$$R_L = 4k\Omega \tag{3.16}$$

also, the two center frequencies are:

$$\omega_1 = 2\pi \times 300MHz \tag{3.17}$$

$$\omega_2 = 2\pi \times 437MHz \tag{3.18}$$

Using our derived formulas to derive component values and simulating the resulting circuit results in the reflection coefficient plot shown in Figure 3.6. The two matching frequencies are clearly visible in the response. The matching network circuit was made using discrete components as seen in Fiure 3.5. An Agilent N9020 network signal analyzer was

32
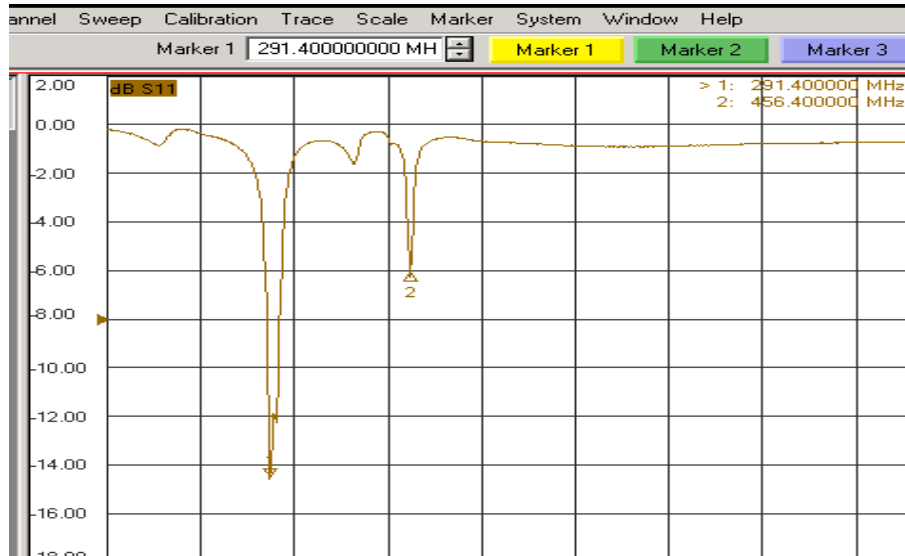
Figure 3.7: **Refleciton coefficient measurements on the matching network.** The network demonstrates less than 6dB reflection at the two passbands located at frequencies 291.4MHz and 456MHz.

used for the reflection coefficient measurements shown in Figure 3.7.

Comparing Figures 3.6 and 3.7 demonstrates the effectiveness of our proposed method. The slight shift in frequencies is largely due to extra parasitics introduced by board elements.

3.5   Summary

In this chapter presented a novel dual-band matching network based on a Chebyshev filter. It was shown that the proposed approach is able to match the dual-resonator tank to a known source resistance at desired frequencies. Simulation and measurement results showed that the matching network provides the required performance.

CHAPTER 4

Circuits for an Intraocular Pressure Sensor

4.1 Motivation and Related Work

LOW power microsystems have become possible today due to advances in low-power integrated circuit design, improvements in fabrication technology, and evolution of more efficient low-profile energy sources. Many biomedical applications can benefit from such microsystems. In this chapter, we focus on one specific application, Glaucoma diagnosis and management. Glaucoma is the second-leading cause of blindness, affecting over 60 million people worldwide and is predicted to impact nearly 80 million by 2020 [49]. As the disease progresses, peripheral vision worsens, reducing the field of view until vision is permanently lost. Elevated intraocular pressure is currently the only factor used to diagnose or control the disease. Glaucoma begins gradually, with many patients unaware of it until a visit to an ophthalmologist. Tonometry is typically used to infer intraocular pressure from the deflection induced by applying a force to the cornea. This non-invasive indirect technique assumes an average thickness, rigidity, and curvature for the cornea, although these parameters vary from person to person. Furthermore, intraocular pressure also varies based on physical activity and diurnal variations that cannot accurately be captured in the doctors office [2]. Once glaucoma has been detected, frequent tracking of intraocular pressure becomes even more important in controlling the progression of the disease, but this requires frequent visits to a healthcare facility. An implantable intraocular microsystem could solve this problem, providing continuous monitoring of pressure fluctuations regardless of activity or

time of day, and affording increased accuracy compared to conventional tonometry. Patient compliance and drug efficacy are additional useful outcomes for physicians treating patients with glaucoma.

The ophthalmological community recognizes the benefits and challenges of continuous IOP monitoring, motivating previous work in this area [2]. A demonstrated device allows patients to measure their own IOP through a closed eyelid without anesthesia [50]. This procedure uses tonometry and is convenient for frequent monitoring. However, it creates additional inaccuracies and requires extensive patient intervention. A contact lens approach measures IOP by measuring the deformation of the cornea curvature due to IOP changes [51]. This reduces patient intervention, but requires an external power source from an eye patch surrounding the eye of the patient. Typical usage is limited to a 24 hour time period. A more invasive approach embeds a pressure sensor within a replacement lens [52]. This provides a more direct measurement of IOP over a longer time period than the contact-lens solution, but requires lens replacement for patients who otherwise may not need it. IOP monitors can be implanted in the anterior chamber of the eye to perform long-term monitoring with minimal invasiveness and low patient intervention (Figure 4.1). A passive 4 mm x 1 mm externally-powered monitor has been demonstrated, measuring instantaneous IOP with 1 mmHg resolution but may impede the field of view [53]. An on-board power source can allow implantable microsystems to track Circadian rhythms in IOP without per-measurement patient intervention for power transmission. Including a large antenna with these monitors allows them to be inductively powered and improves data transmission, but may complicate implantation procedures. One such approach described a 2.3 μW monitor that measures IOP with 0.9 mmHg accuracy and uses a 1 cm PCB loop antenna [54]. Another recent implanted solution stores energy on a 24 μF capacitor array to continuously collect data over a 24 hour period, but requires a 27 mm antenna for data and power transfer [55].

One primary factor that distinguishes the proposed intraocular pressure sensing microsystem (IOPM) from previous work is its small 1.5 mm^3 form factor that enables us to implant in the Anterior Chamber of the eye (Figure 4.1). From a circuits perspective, the major challenge is to design all the system components such that they do not exceed the power budget of the system. Table 4.1 shows the main circuit-level limitations on the system. In
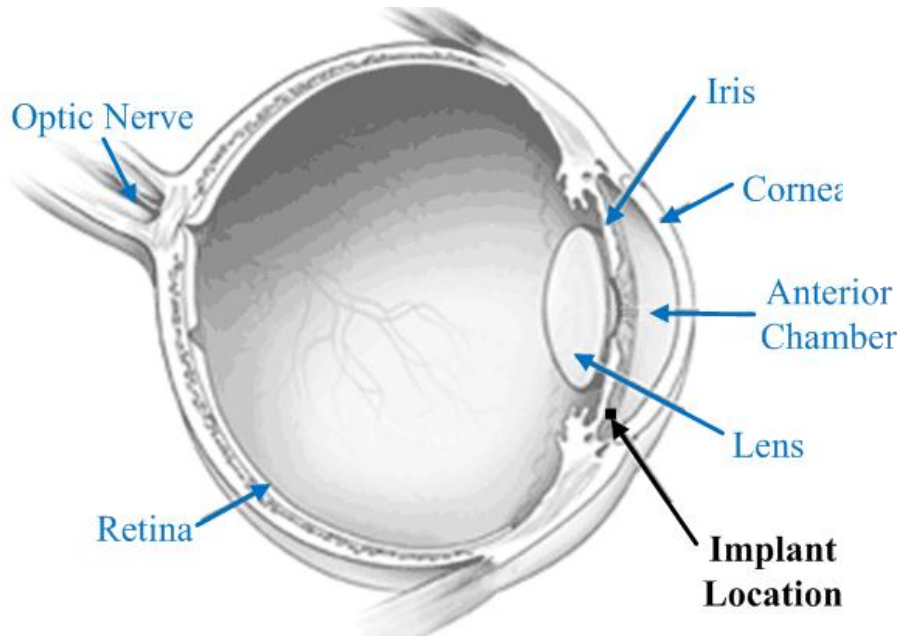
Figure 4.1: **The 1.5 mm^3 IOP monitor is implanted in the anterior chamber of the eye as part of a treatment for glaucoma.**

Table 4.1: **Circuit Constraints on IOPM.**

Module	Requirement	Achieved
CDC Sensitivity	1 mmHg	0.5 mmHg
CDC Active Power	10 μW	7 μW
Radio Energy/bit	7 nJ/bt	4.7 nJ/bit
Total Stand-by Power	5 nW	3.3 nW
Total Silicon Area	1.8 mm^2	1.8 mm^2

order to realize these goals, we introduce novel blocks with record-low energy consumption and apply analog and digital low-power techniques to other blocks to keep average and peak power consumption below the values dictated by the small thin-film battery.

4.2 Intraocular Pressure Sensor Overview

4.2.1 Implantation

In this chapter, we present circuits for a 1.5 mm3 IOP monitor. The microsystem is designed for implantation on the surface of the iris, enabling long-term IOP monitoring with wireless data transmission and self-powered energy-autonomous operation (Figure 4.2).
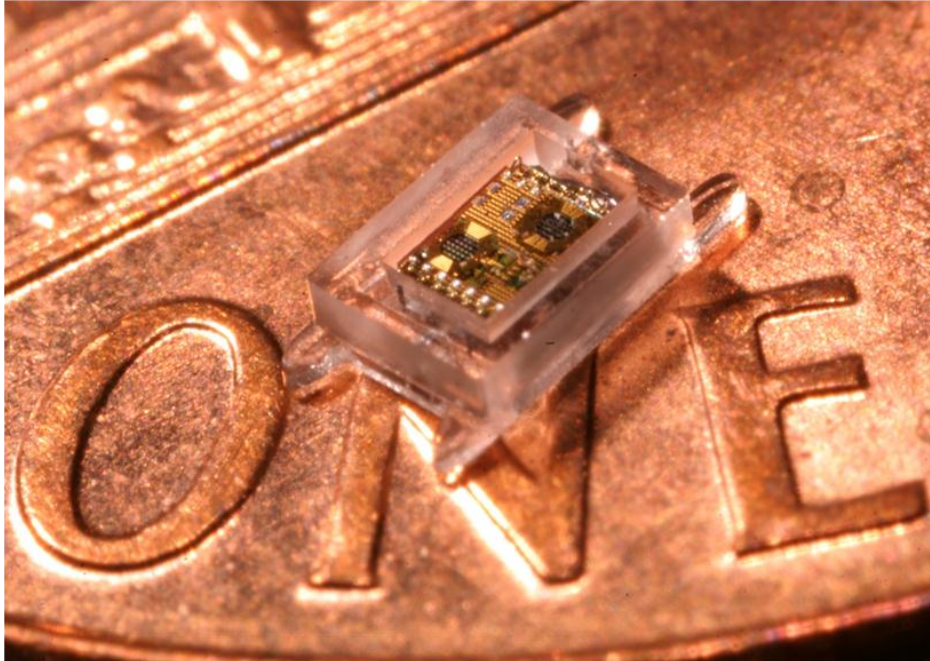
Figure 4.2: **IOP monitor microsystem photo. The top of the glass enclosure is omitted to highlight circuit components.**

Due to the small system size a minimally-invasive surgical procedure, modeled after typical cataract surgery, can be used to implant the device onto the surface of the iris. The targeted implant location allows physicians to observe the device after implantation and also reduces the required wireless transmission distance. The implant procedure requires no sutures since the incision is self-healing, and the device is designed to allow for easy explantation with minimal tissue damage if the need to remove the microsystem arises. Haptics built into the package fix the device in position using the natural elasticity of the tissue [56].

In order to reduce the chance of damaging the cornea, the overall device thickness is limited to 0.5 mm. The length and width are set by the maximum dilation of the pupil so that the field of vision is not compromised.

4.2.2   System Structure

Any intraocular implant is severely constrained by the available volume, so the packaging and overall structure of the microsystem are critical design issues. The vertically-stacked structure used in this high-density microsystem protects the electronics from body fluids
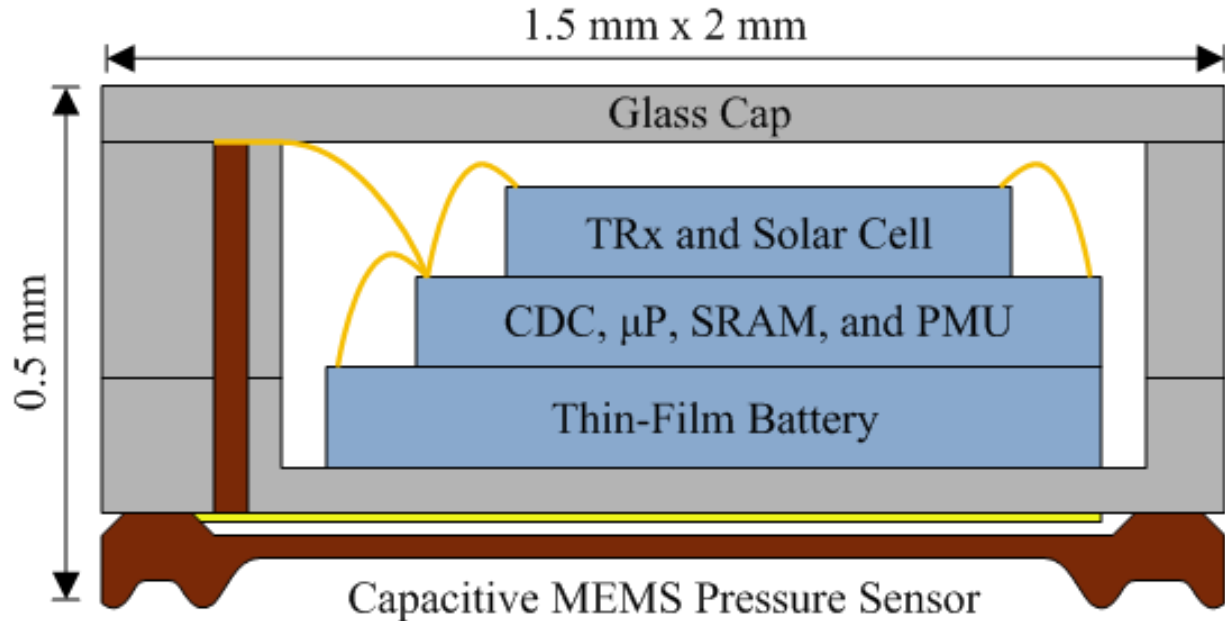
Figure 4.3: **The IOP monitor includes two ICs and a battery, encapsulated within a biocompatible glass housing. Vertically-integrated silicon feedthroughs provide connection to the externally-mounted capacitive MEMS pressure sensor.**

while simultaneously minimizing unused space (Figure 4.3). The monitor contains two integrated circuit (IC) chips fabricated in a 0.18 μm CMOS process. The top IC contains a solar cell and fully-integrated wireless transceiver (TRx). The bottom IC contains a sigma-delta capacitance to digital converter ($\Sigma\Delta$ CDC), microprocessor (μP), and static random access memory (SRAM). The solar cell and a thin-film solid-state Li battery deliver power to the microsystem through the power management units (PMU), allowing microsystem operation without patient intervention for power delivery. The ICs and battery are placed within a specially-designed cavity in a glass housing. On the external surface of the glass, a thin boron-doped silicon diaphragm is anodically bonded forming a hermetically-sealed capacitive pressure sensor. Vertical interconnects through the glass provide direct electrical connections to the sensor [57]. Ambient light is used for energy harvesting, and wireless communication signals easily penetrate the package to form a bidirectional interface with the outside world. The pressure sensor, circuits, and glass housing are fabricated using scalable CMOS and MEMS techniques.

4.2.3 Usage Model

Based on ophthalmological and circuit constraints, the monitor samples IOP every 15 minutes, representing continuous monitoring of this slowly-changing biological signal [58]. The measurement interval is set with a programmable leakage-based timer located in the bottom wakeup controller (bottom WUC) (Figure 4.4) [59]. When the timer expires, the $\Sigma\Delta$ capacitance to digital converter measures absolute IOP, which is calibrated against an external pressure measurement to determine the IOP relative to atmospheric pressure. The capacitance to digital converter monitors a capacitive pressure sensor and stores a 14b digital representation of the pressure data. After completing the pressure measurement, the microprocessor wakes up, retrieves the recently recorded IOP data from its memory-mapped location, performs digital signal processing, and then logs its result into SRAM. The microsystem then enters standby mode until the next IOP measurement or user-generated event, with a power of 3.72 nW at room temperature.

The microsystem includes a receiver for wireless querying of IOP data. The doctor or patient places a handheld external wand over the eye. The wand transmits a wireless radio-frequency (RF) signal to the monitor, located on the surface of the iris. The IOP monitors transceiver detects this signal and activates a microprocessor program that retrieves logged data from SRAM and coordinates the transceiver as it sends data to the external wand. After a data transmission, the microsystem enters the nW standby mode to conserve power until the next event.

The microsystem operates using zero net energy for an indefinite lifetime using a combination of solar energy harvesting and ultra-low-power operation. The solar cell provides a 0.5 V power source (VSOLAR), which is used to recharge the 3.6 V battery (V3P6) with 80nW. Voltage up-conversion is performed with a fully integrated switched capacitor voltage regulator (SCVR) located in the power management unit. The microsystem conserves energy by using aggressive low power circuit design techniques. Weak inversion biasing limits quiescent current in the 7.0 μW sensor interface electronics. Short 100 ns transmit pulses limit the energy used in the 4.7 nJ/bit transmitter by reducing the time that the transceiver draws power from the battery. Near-threshold processing reduces microprocessor
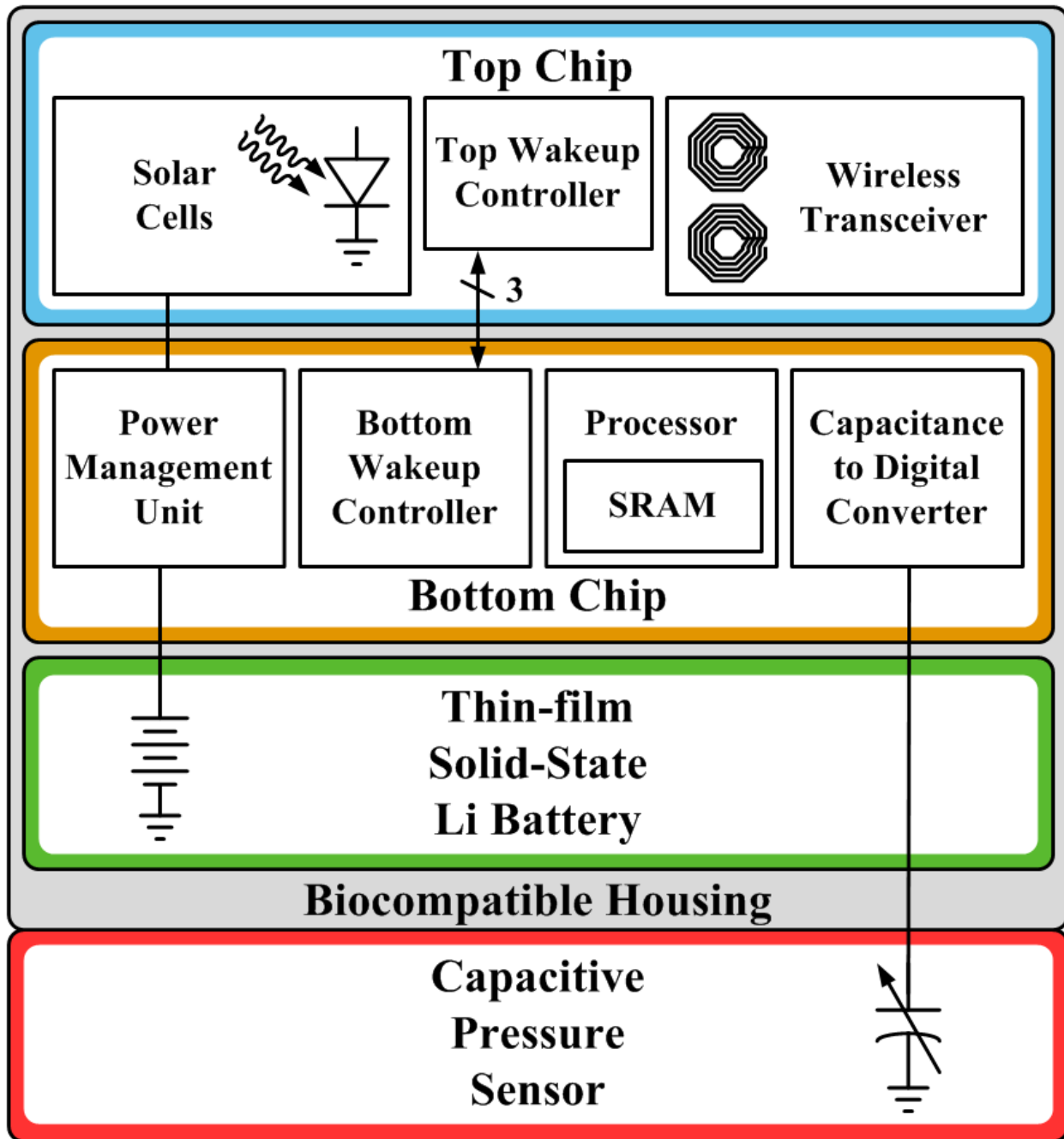
Figure 4.4: **IOP monitor block diagram.**

and SRAM active mode energy to 90 nW. Power gating, gate length biasing, and careful device flavor selection minimize microprocessor and SRAM standby mode power to 72 pW. The same switched capacitor voltage regulator used for energy harvesting delivers power to the low-voltage digital circuits (V0P45) with 75% active mode and 40% light-load standby mode efficiencies. With the intended usage model, these circuit techniques described in the remainder of this paper enable the microsystem to be energy-autonomous with 1.5 hours of sunlight per day, with a 1 month battery lifetime without recharging.

4.3   Capacitance to Digital Converter

4.3.1   Capacitance to Digital Converter Background

Capacitance to digital converters (CDCs) apply an excitation force to a variable sensor capacitance to generate a voltage, current, or time and then use analog to digital converters (ADCs) to output a digital value. Simple readout circuitry charges and discharges the capacitance with a CMOS ring oscillator, and measures the oscillation frequency. However, this method is highly dependent on process, voltage and temperature variations. A 500 μW capacitance to digital converter design incorporates the sensor capacitance into the digital to analog converter portion of a successive approximation register (SAR) ADC [60]. SAR ADCs have been demonstrated with figures of merit as low as 4.4 fJ/conversion step in a 1.9 μW design [61]. Several capacitance to digital converter designs incorporate the sensor capacitance as a switched-capacitor resistor in an integrating amplifier to achieve accuracies within 19.3 aF [62–64]. The slope of the integrator output is proportional to the pressure sensor capacitance. The integrator output ramp can be digitized using $\Sigma\Delta$ or pulse-position modulation (PPM) ADCs, with a demonstrated 5.6 μW $\Sigma\Delta$ ADC achieving 303 fJ/conversion step [65] and a 14 μW PPM ADC achieving 98 fJ/conversion step [66]. The 7.0 μW $\Sigma\Delta$ capacitance to digital converter in this IOP microsystem saves power by applying excitation forces to the measured capacitance with weakly inverted devices and eliminating the integrating amplifiers found in typical $\Sigma\Delta$ converters.
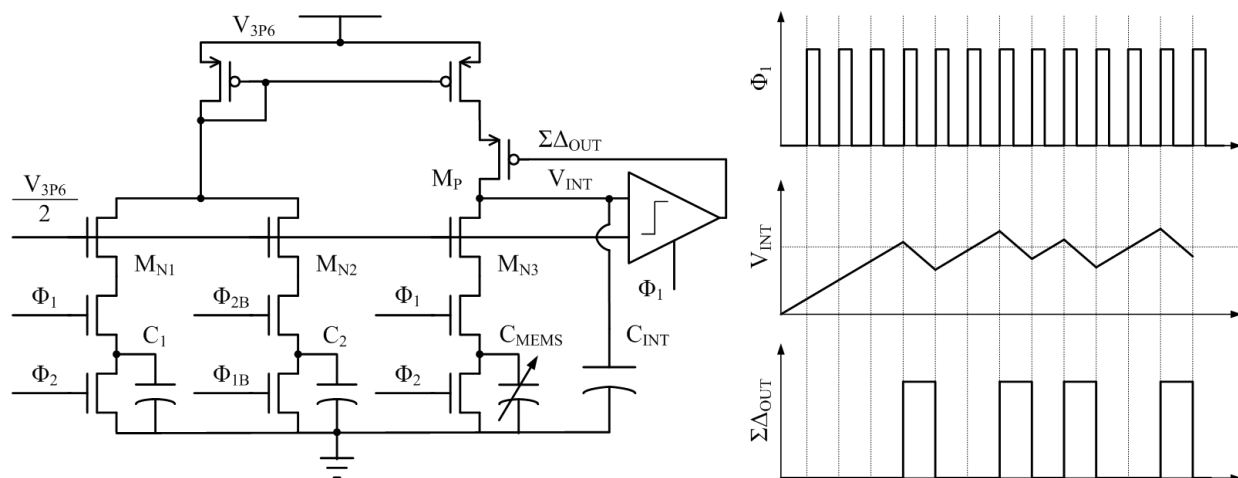
Figure 4.5: **The capacitance to digital converter generates a pressure-sensitive current by switching the pressure sensor and measures the pressure sensor capacitance with $\Sigma\Delta$ modulation.**

4.3.2 Capacitance to Digital Converter Implementation

The capacitance to digital converter compares the capacitance of the pressure sensor (CMEMS) and 250 fF MIM capacitors (C1, C2) (Figure). Pressure-sensitive and fixed resistances are generated by switching CMEMS, C1, and C2 using shared 50 kHz non-overlapping clocks (1, 2). C1 and C2 use 180 ° out of phase clocks to create a near-constant fixed resistance. This method yields better results than switching a single 500 fF MIM capacitor. Since the clock is shared between the resistances, the capacitance to digital converter output has reduced sensitivity to clock uncertainty. A fixed voltage is dropped across the switched-capacitor resistors to generate both a pressure-sensitive and a fixed current. This voltage drop is regulated with saturated transistors MN1, MN2, and MN3. A reference voltage equal to V3P6/2 is generated using a 2:1 switched capacitor divider and connected to the gate of the current limiting devices. Since V3P6/2 is shared, the capacitance to digital converter output also has reduced sensitivity to V3P6.

The pressure-sensitive current discharges an integrating capacitor (CINT). Simultaneously, the fixed current is selectively integrated onto CINT using $\Sigma\Delta$ modulation. This integration method does not require an amplifier, avoiding the power overhead for its quiescent current. $\Sigma\Delta$ modulation cancels out quantization noise and temporal noise allowing

higher accuracy with lower power circuits. The voltage on CINT (VINT) is compared with V3P6/2 using a clocked comparator. The current values are chosen such that VINT increases when both currents are integrated. When VINT exceeds V3P6/2, the comparator output ($\Sigma\Delta_{OUT}$) goes high and blocks the fixed current using device MP1, causing VINT to decrease. The fixed current is enabled again when VINT drops below V3P6/2. In this method, VINT is regulated near V3P6/2 with a duty cycle on $\Sigma\Delta_{OUT}$ that is equal to the ratio of the pressure-sensitive and fixed currents. This data stream is accumulated into a 14b digital value with a 10,000:1 decimation filter that counts the number of cycles where $\Sigma\Delta_{OUT}$ is high over a 10,000 clock cycle period.

The following low power techniques in the capacitance to digital converter decrease overall IOP energy usage and reduce the amount of harvested energy required for energy autonomy. The microsystems battery can supply at most 40 μW, so to reduce power the capacitance to digital converter generates a 0.9V 50 kHz clock with a current-starved ring oscillator, and then converts it to a 3.6 V clock for the switched capacitor resistors and comparator. The slow clock decreases the pressure-sensitive and fixed currents and also reduces the activity and power of the comparator. However, since capacitance to digital converter accuracy is related to the number of clock cycles, using a slower clock does not reduce the energy per measurement. Energy per measurement is inversely related to clock frequency because of increased leakage energy over a longer measurement time period. Between pressure measurements, the clock is disabled and only leakage power is consumed. To reduce leakage power, all transistors in the capacitance to digital converter are high threshold voltage, thick-gate oxide input-output (I/O) devices with leakage power that is three orders of magnitude lower than logic devices leakage.

4.3.3 Capacitance to Digital Converter Measurement Results

The MEMS capacitive pressure sensor is placed in a pressure chamber and connected to the capacitance to digital converter for measurement. The pressure range of interest for IOP measurements is 0-60 mmHg above atmospheric pressure, with healthy IOP ranging between 10-21 mmHg. Higher pressures can indicate glaucoma [11]. The pressure sensor
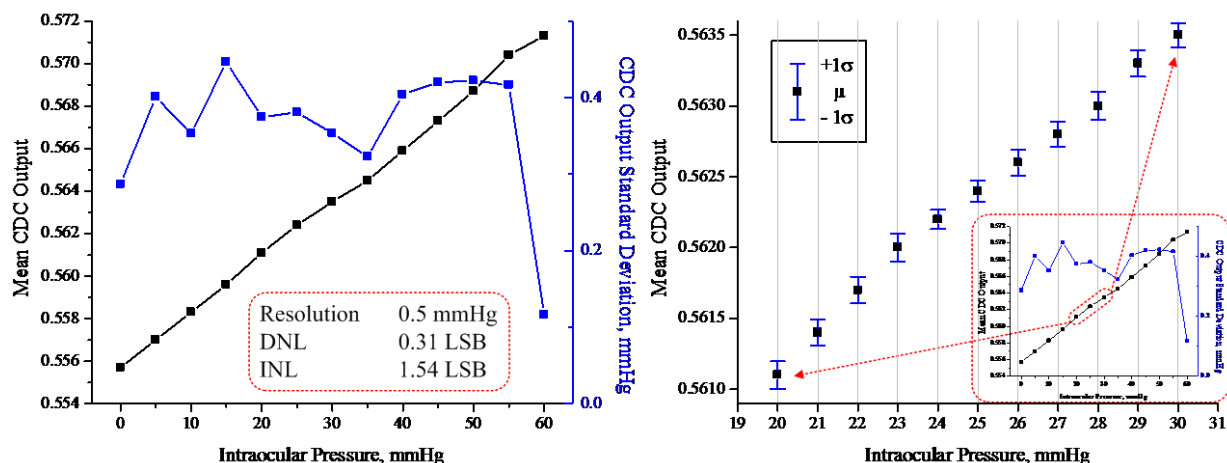
Figure 4.6: **The pressure sensor and capacitance to digital converter achieve 0.5mmHg IOP accuracy with high linearity.**

has a resolution of 26 fF/mmHg with high linearity [10]. Pressure sensor hysteresis effects contribute 1mmHg of uncertainty to the pressure measurement. Goldmann applanation is the golden standard for IOP measurements and achieves 1 mmHg accuracy. The capacitance to digital converter has 0.5 mmHg accuracy, equivalent to a resolution of 13fF, while consuming 7.0 μW active and 173 pW standby power (Figure 4.6). The standard deviation is less than 0.5 mmHg with 50 measurements taken at each pressure. The output is highly linear due to the contact-mode pressure sensor and switched-capacitor capacitance to digital converter techniques. The differential non-linearity (DNL) is 0.31 LSB and the integrated non-linearity (INL) is 1.54 LSB, calculated using end point linear calibration.

Although body temperature is well controlled, the outer eye does experience some temperature fluctuations on the order of 10 °C [67]. To reduce temperature sensitivity, the capacitive sensor is sealed in vacuum to mitigate the effects of thermal expansion. The fixed MIM capacitors in the capacitance to digital converter also exhibit low temperature dependence. The temperature sensitivity of the capacitance to digital converter is 5.6 mmHg / °C as shown in Figure 4.7. From reference [67], we expect the temperature at the surface of the iris to vary between 15°C and 40°C in extreme external environments. This error due to temperature variations would need to be calibrated out with an external temperature measurement. Measurements of the pressure sensor used in this work indicate drift of less than 0.5mmHg over the course of 2 weeks. Long-term in vivo sensor drift studies would be
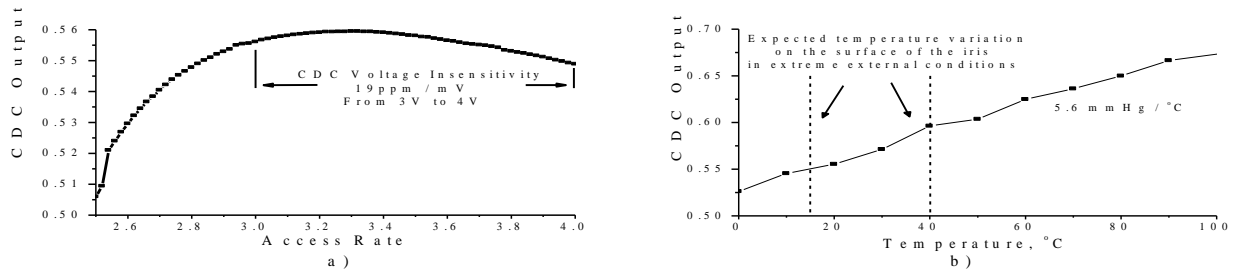
Figure 4.7: **Pressure measurement sensitivity to variations.** a) Battery voltage variations b) Temperature Variations.

useful in assessing the impact of scar tissue build-up on the sensor on IOP measurements.

4.4 Microprocessor and Memory

4.4.1 Microprocessor and SRAM Background

There has been significant previous work on low-power microprocessors and SRAM. VDD scaling reduces dynamic energy quadratically and leakage power super-linearly. However, delay degrades resulting in increased leakage energy per microprocessor instruction. The competing trends in dynamic and leakage energy lead to an intermediate near-threshold or sub-threshold VDD where total energy per instruction is minimized [68–70]. Numerous designs have applied VDD scaling to custom and commercial microprocessors to achieve energy as low as 2 pJ per instruction [71, 72]. To ensure low-VDD functionality, previous works remove high fan-in standard cells and perform extensive Monte Carlo analysis of sequential elements [71, 73]. When inactive, the microprocessor consumes only leakage power. Optimal technology selection balances active and standby energy for the microprocessor based on its duty cycle [74]. Power gate size should be chosen to minimize leakage while meeting performance requirements, which are often loose in ultra-low power sensor applications [73]. The power gate can be implemented as a low-leakage I/O device and then overdriven with VBATT to maximize on-to-off current ratio [75].

Processor data can be stored in volatile or non-volatile memories. Non-volatile memories such as embedded Flash do not require power to retain data, making them good candidates for reducing standby mode power [76]. However, these memories have high write powers,

require high write voltages, and are not readily available to academic researchers. SRAM is easily designed in CMOS processes using only the nominal voltage. However, data retentive SRAM cannot be power gated without data loss, so minimizing SRAM leakage is vital for achieving energy-autonomy. VDD scaling in SRAM reduces energy but degrades stability margins [77]. An 8T SRAM bitcell separates read and write constraints to improve stability [78, 79]. A 10T SRAM approach further improves read stability by pulling up read bitlines (BLs) and reducing read buffer leakage [80, 81]. The microsystem includes a 9.8 pW 0.45 V 4kb ultra-low-leakage 10T SRAM. The SRAM bitcell uses I/O devices and gate length biasing in the data-retaining portion while power gating the read buffer to achieve 2.4 fW/bit standby leakage [82]. The SRAM drives the BLs at 0.9 V to improve write stability, and employs PMOS pass gates because they are faster at the VDD of interest and hierarchical BLs to reduce latency.

4.4.2 Microprocessor and SRAM Implementation

The microprocessor coordinates data transfer and management among the capacitance to digital converter, wireless transceiver, and SRAM. After a capacitance to digital converter measurement is complete, the microprocessor wakes up from standby mode and reads the result from a memory mapped location. The microprocessor can perform digital signal processing (DSP) to extract useful medical information from raw IOP data as well as perform data compression. Simple examples of DSP include detection of the average, peak, or changes in IOP over a time interval. This analysis is facilitated by the linear relationship between pressure and capacitance to digital converter output. The microprocessor can also be used to compress IOP data, reducing memory footprint. The full-range capacitance to digital converter output ranges from 0-10,000 with a 14b digital representation. However, over the pressures of interest, the output range is 180 allowing the microprocessor to compress the data to an 8b value. Storing differential instead of absolute IOP values further reduces memory footprint, enabling leakage reductions through power gating of unused SRAM banks during standby mode. After processing the data is stored into SRAM. When the user generates a wireless wakeup event, a separate microprocessor program is called. This program

receives wakeup signals from the transceiver, retrieves data from SRAM, and initiates wireless transmissions.

Low-power techniques in the microprocessor and SRAM reduce active mode peak power and standby-mode-limited energy consumption. The microprocessor is an 8b microcontroller with an instruction set that supports 16 registers. In the 8b instruction, 4 bits are an instruction operand. For 15 operands, the other 4 instruction bits denote a register. These instructions compute operations between the designated register and a general purpose register that is used in every instruction. The 16th operand performs special tasks based such as initiating a transceiver transmission and entering standby mode. VDD is scaled to near the minimum energy point, achieving 90 nW power consumption at 0.45 V. In standby mode, an NMOS I/O header virtually eliminates the microprocessors contribution to standby mode power. In active mode, this header is overdriven with VBATT to meet the 100 kHz performance target.

4.5 Wireless Transceiver

4.5.1 Transceiver Background

Wireless transceivers for medical implants are limited by antenna size and power budget constraints. Passive backscattering techniques bypass transmitter power budget limitations by reflecting an incoming RF signal using impedance modulation. These techniques achieve a 10-6 transmit bit error rate (BER) over a 2 cm transmission channel with a 3.5 cm diameter coil [83] and a 1.510-6 BER over 15 mm with a 40 mm coil [84]. However, these devices are too large for IOP monitoring. Active techniques draw from microsensor power supplies to achieve higher transmit performance with smaller antennas or coils. These transmitters achieve energy efficiencies as low as 20.4 nJ/bit with coils as small as 0.47 mm [21, 55, 85]. Previous transceiver implementations and the transceiver for this IOP monitor all consume higher peak power than the $1mm^2$ battery can source and limit device lifetime because of high leakages. In this transceiver design, energy per data transmission is limited by reducing the transmitter active time to 100 ns/bit. The transmit energy is supplied from charge

reservoir generated with 1.6 nF of integrated capacitance. Finally, low-leakage IO devices with reduced sizes limit leakage power while meeting performance targets.

4.5.2 Transceiver Implementation

The fully-integrated transceiver receives wireless wakeup signals and responds with IOP data. It uses FSK modulation with two tones at 433 MHz and 915 MHz in the industrial, scientific, and medical (ISM) bands. The doctor or patient places an external wand over the eye and transmits a wireless wakeup signal to activate the IOP monitor. The receiver is activated (RxEN) and generates one of two digital signals (Rx0, Rx1) based on the wakeup signal frequency (Figure 4.8). The wakeup signal is coupled onto one LC tank of the dual-resonator structure and connected to the rectifier with a switch controlled by RxEN. The ac signal is converted to dc using one of two 8-stage full-bridge rectifiers. The dc offset is then converted to the digital Rx0 and Rx1 signals by comparing the dc outputs of the rectifiers with two 50Hz variable-offset comparators. Thus, the Rx0 or Rx1 is generated when more RF energy is received on either half of the dual-resonator tank than the other, indicating a wakeup signal at the intended frequency. These digital signals are sent to the top wakeup controller (top WUC), which coordinates communication with the microprocessor. The microprocessor receives signals from the top wakeup controller and responds by issuing commands to the top wakeup controller. The top wakeup controller determines what data to transmit (Tx0, Tx1) and enables the transmitter (TxEN) to send medical data to the external wand.

The transceiver uses a dual-resonator LC tank [36]. The dual-resonator allows higher frequency separation between the FSK tones compared to a single LC tank using a varactor, mitigating phase noise degradation . It is formed by the series connection of two LC tanks (L_0C_0, L_1C_1) that are tuned to 433 MHz and 915 MHz. It resonates when a wireless signal at either of these frequencies is sent to the IOP monitor, with the ac signal developed across the corresponding LC tank. Therefore, the receiver can detect two wakeup signals to initiate separate microprocessor procedures or program the IOP monitor. Differential analysis of the received ac signals reduces the false wakeup rate from noise outside of the
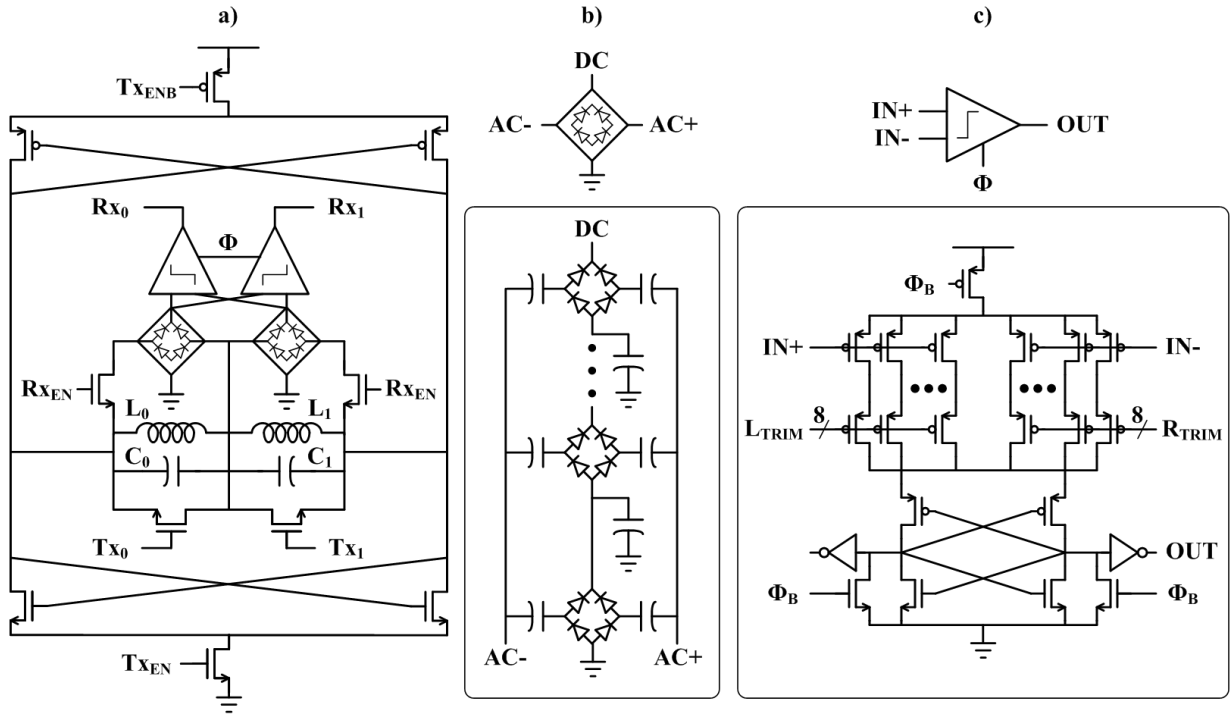
Figure 4.8: **Transceiver schematics.** a) Combined local oscillator and power amplifier b) Multistage rectifier c) Variable offset comparator.

resonance frequencies. The dual-resonator transmits data by shorting one LC tank, enabling the oscillator, and radiating power from the inductor coils. It achieves high tone separation with 10% lower circuit area than two separate LC oscillators.

Wireless wakeup signals are detected by rectifying AC signals that are coupled onto the dual resonator. The ac signals are converted to a dc voltage using 8 full-bridge rectifier stages. Each half of the dual resonator is ac coupled to each of its associated rectifier stages, where Schottky diodes generate a dc potential. The output of the 8-stage rectifier is converted to a full swing digital signal using a clocked comparator. This comparator runs continuously in standby mode, so it must be low power to meet the microsystems energy budget. The comparator runs with a 31 pW 50 Hz clock that is generated at 0.45 V using a leakage-based oscillator [59] and then level-converted to the 3.6 V comparator input.

The transmitter uses an architecture that combines the local oscillator (LO) and power amplifier (PA). This modification is necessary to reduce circuit area by including fewer fully-integrated inductors. For PA functionality, the inductors need to be large to radiate enough

power for the external wand to detect. However, the 0.41 mm diameter, 5-turn coils degrade LO phase noise because of low quality factor (Q). The Q of the inductors is further degraded by placing solar cells underneath the coil openings to save area. The effects of lower Q on phase noise are mitigated by using the dual-resonator with high frequency separation between tones.

During data transmission, the transceiver requires greater peak power than the battery can supply. Therefore the transceiver draws instantaneous power from a local charge reservoir. The local charge storage is implemented as 1.6 nF of integrated metal oxide semiconductor (MOS) and MIM capacitance on the ICs. The transceiver sends a single 100 ns pulse at a time, which degrades the voltage on the local supply by less than 25%. The local supply is then recharged for the next 131 μs from the battery, using a resistor to prevent high currents from damaging the battery, resulting in an effective data rate of 7.5 kb/sec (Figure 4.9). The transmitter can send daily IOP data taken every 15 minutes in 130 ms.

4.5.3 Transceiver Measured Results

The transceiver is tested in a laboratory using an external wand to communicate with the IOPM. The wand contains PCB-trace inductors and matching networks connected to an RF signal generator and spectrum analyzer to transmit and receive data [86]. An optimized wand would contain a transceiver made of commercial-off-the-shelf components instead of relying on the signal generator and spectrum analyzer, and would achieve a lower noise floor. The transmit media between the IOP monitor and wand is air as well as 0.5 mm of saline to model the aqueous humor and cornea. The IOP monitor is demonstrated to wake up when a 1W wireless signal is sent at a distance of 4mm. After receiving this signal, the IOP monitor will respond by transmitting data to the wand with a BER of 10^{-6} at a distance of 10cm. The transmit BER vs. transmission distance is shown in 4.10.

In order to demonstrate system operation, the radio was implanted in a mouse as shown in Figure 4.11. The external wand receives the signal using a PCB coil. The received signal is amplified, filtered, and down-converted using a spectrum analyzer to reconstruct the transmitted waveform. Figure 4.11 also shows the successful reception of transmitted
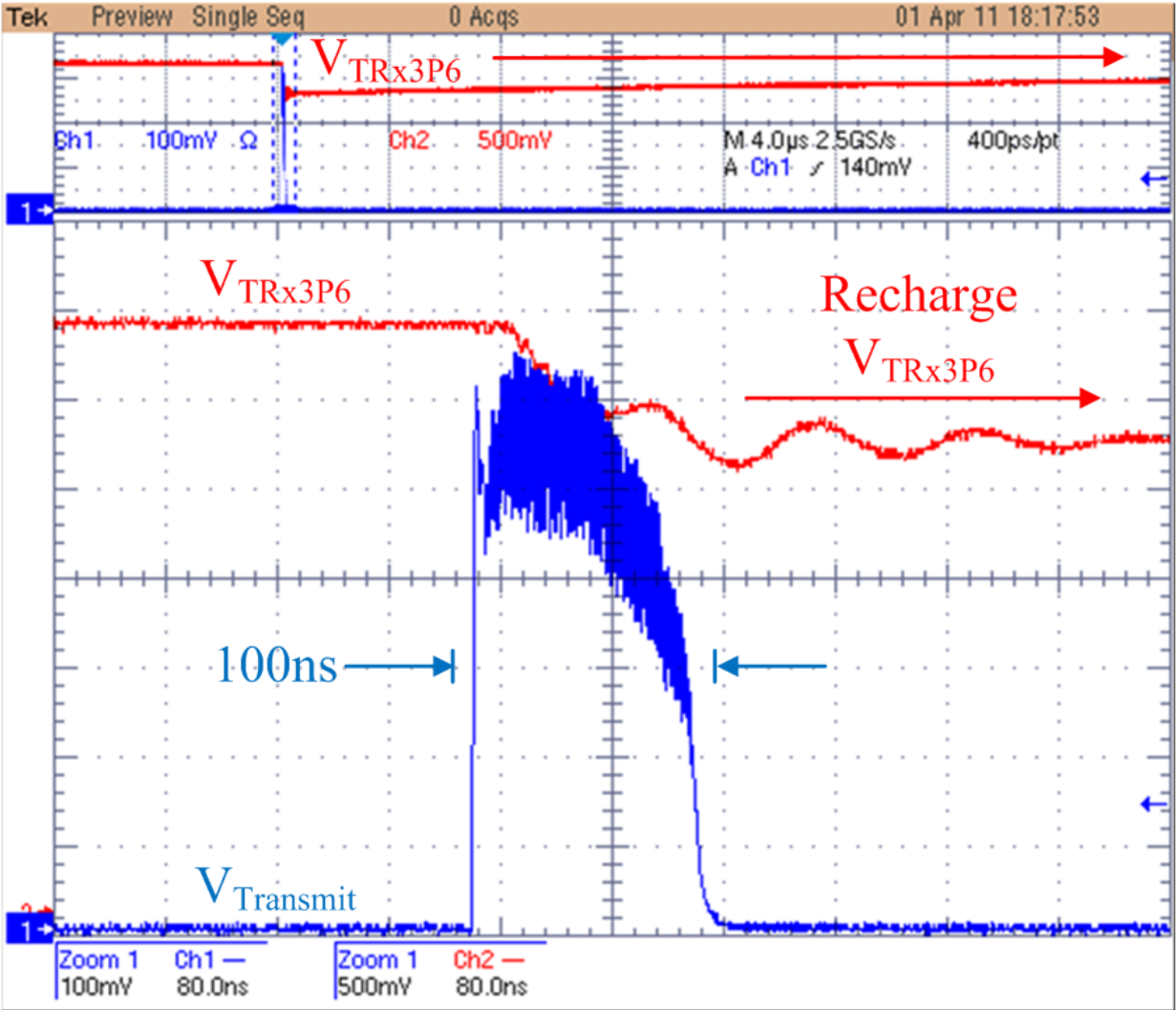
Figure 4.9: **Received signal from the transceiver.**
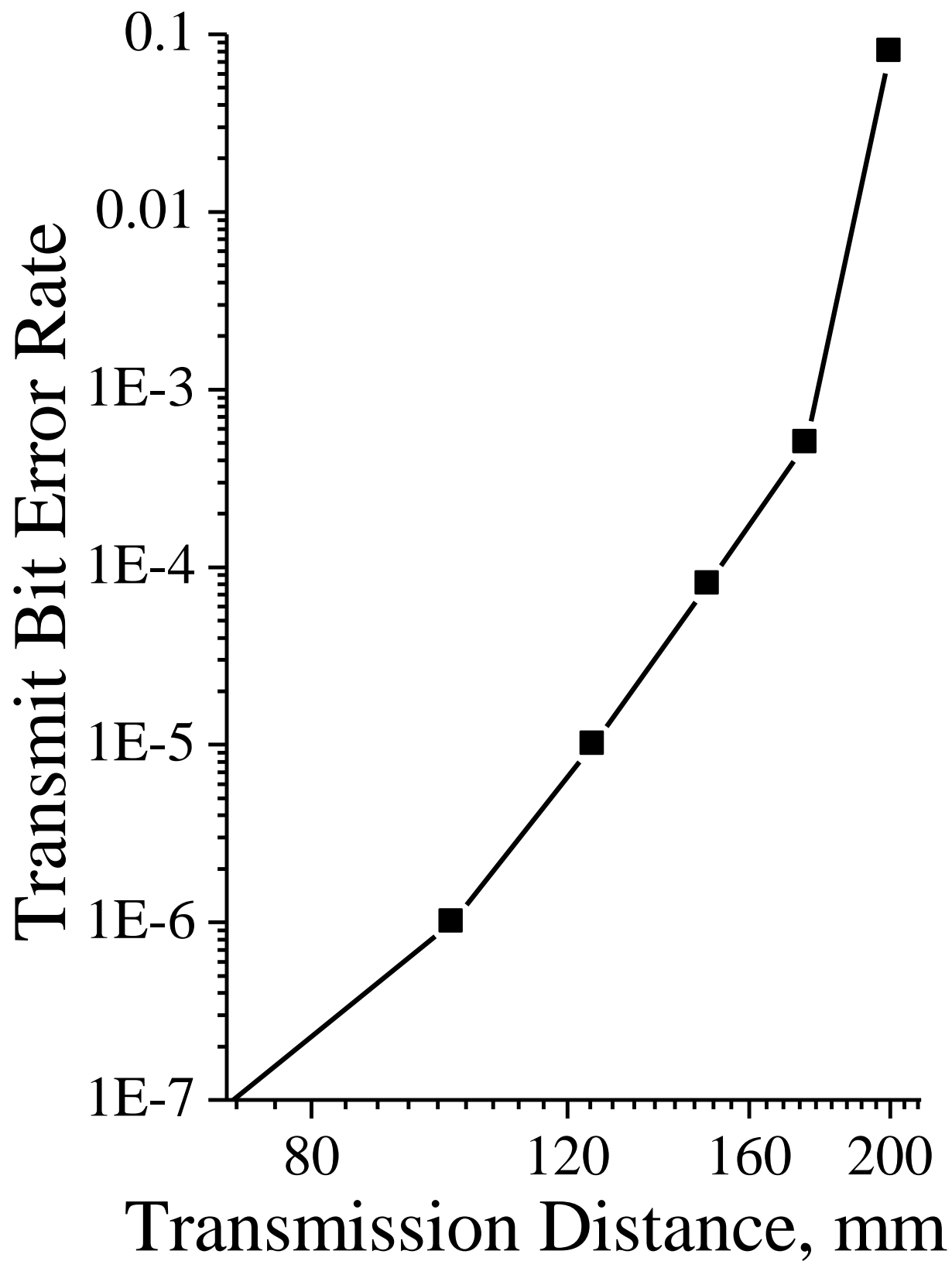
Figure 4.10: **Transmitter BER plot.**
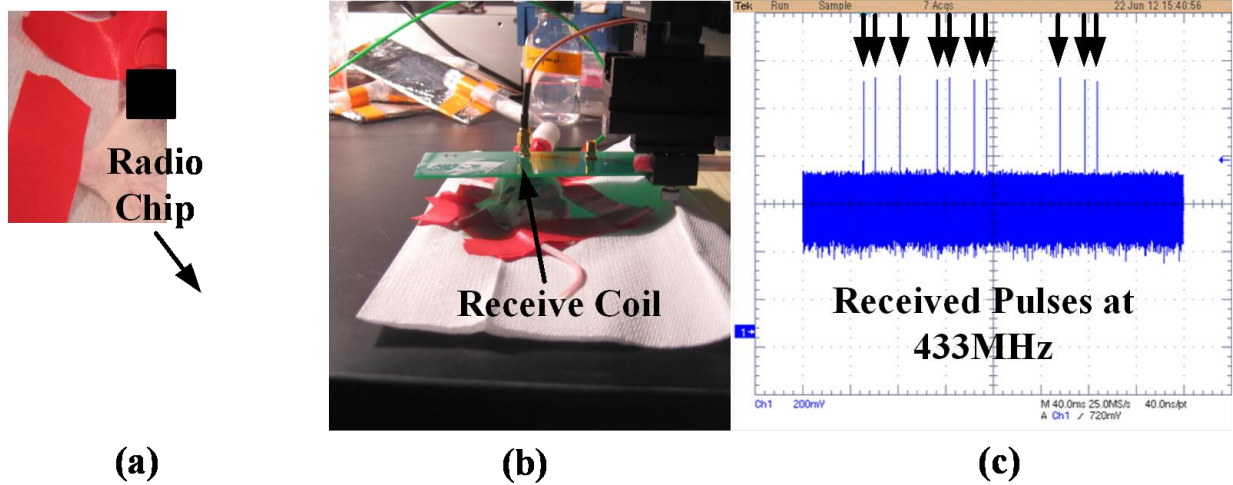
Figure 4.11: **Transmitter in-vivo measurements.** a)In-vivo radio testing implantation b) Measurement setup c) Received pulses at 433MHz.

data in the implanted system.

4.6 Energy Autonomy and Power Breakdown

The power management unit recharges the battery from the solar cell and delivers power to load circuits (Figure 4.12). The solar cell size is limited to 0.07 mm2 by the size restrictions of the monitor and is fabricated in an unmodified CMOS process using the deep n-well to p-well and p-well to n-active diodes. It is located underneath the transparent transceiver coil openings to save area. The output of the solar cell (VSOLAR) connects to the VDD0P45 node of the switched capacitor voltage regulator. When VSOLAR exceeds 450 mV, the 0.32 mm2 8:1 voltage regulator up-converts the harvested energy to above 3.6 V and recharges the battery. The thin-film solid-state Li battery is supplied by Cymbet Corporation and uses a commercial chemistry, but its size is tailored specifically for this application [87]. V0P45 also supplies the microprocessor and SRAM, allowing the solar cell to directly power the load circuits. When the open-circuit solar cell voltage drops below VDD0P45, the solar cell acts as a load to the microsystem and is disconnected. The open circuit voltage is detected using a small replica solar cell. When V0P45 drops below 0.45 V, power is down-converted from the battery by the same switched capacitor voltage regulator used for energy harvesting
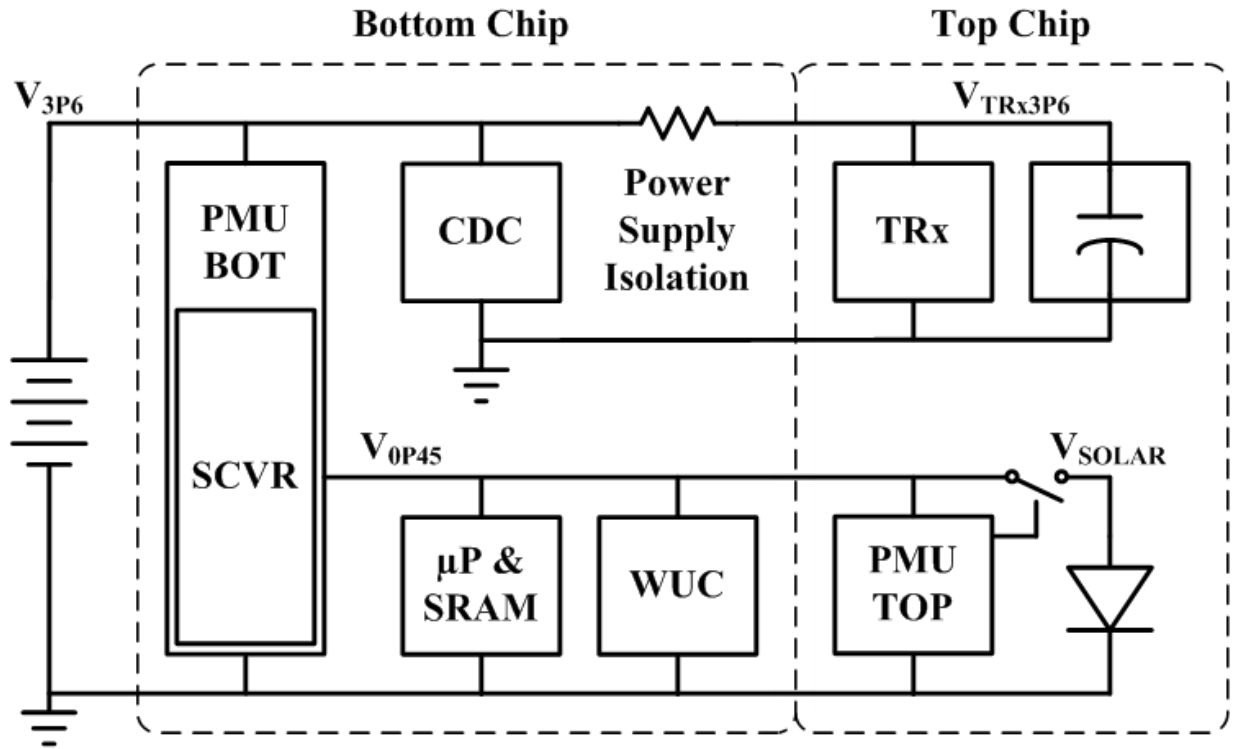
Figure 4.12: **The switched capacitor voltage regulator up-converts solar energy to power the capacitance to digital converter and transceiver, and also recharge the battery. It down-converts stored energy to supply power to digital circuits when there is no solar energy.**

and delivered to the load circuits. Voltage comparisons in the power management unit are performed with clocked comparators that are switched by the switched capacitor voltage regulator and top wakeup controller clocks.

The power management unit is tailored for the microsystems power sources and loads to maximize lifetime. With IOP measurements every 15 minutes, 10,000 microprocessor cycles for DSP per measurement, and daily transmission of 14b raw IOP data, the average microsystem power is 5.3 nW (Table 4.2). Standby transceiver leakage and active capacitance to digital converter power dominate the microsystems energy requirements. The transmitter uses large devices in the combined LO and PA to transmit sufficient power for the external wand to detect. These large devices have 3.3 nW leakage in standby mode even though they are implemented as low-leakage IO devices. The capacitance to digital converter requires 10,000 cycles to achieve the target IOP accuracy of 0.5 mmHg, setting the capacitance to

Table 4.2: **Power breakdown of intraocular pressure sensor microsystem**

Block Name	Power	Time/Day	Energy/Day
Active Mode			
CDC	$7\mu W$	$19.2s$	$134.8\mu J$
TRx	$47.5mW$	$134.4\mu s$	$6.3\mu J$
SCVR	$116.9nW$	$19.2s$	$2.2\mu J$
μ P + SRAM	$90nW$	$19.2s$	$1.7\mu J$
Standby Mode			
CDC	$172.8pW$	$24hr$	$14.9\mu J$
TRx	$3.3nW$	$24hr$	$285.1\mu J$
SCVR	$174.8pW$	$24hr$	$15.1\mu J$
μ P + SRAM	$9.8pW$	$24hr$	$846.7\mu J$
WUP	$62.0nW$	$24hr$	$5.2\mu J$

digital converter energy per measurement. Digital components make smaller contributions to IOP monitor energy usage. In active mode, the switched capacitor voltage regulator delivers power from the 3.6 V battery to the 90 nW 0.45 V microprocessor, SRAM, and wakeup controllers with 75% efficiency. In standby mode, it delivers 72 pW with 40% efficiency.

The IOP monitor achieves energy autonomy by harvesting more energy than it requires for operation. In sunlight with a light irradiance of 1 sun AM 1.5, VSOLAR reaches 500mV, and 80nW is delivered to recharge the battery (Figure 4.13). While these conditions are not typical, in indoor lighting VSOLAR drops to near 460mV and the battery is still recharged with 13nW, more than offsetting the 5.3 nW monitors power consumption. The IOPM requires 10 hours of indoor lighting or 1.5 hours of sunlight per day to achieve energy-autonomy. Energy-autonomy makes the IOP monitor lifetime decades or longer, giving doctors ample time tailor a patient-specific glaucoma treatment.
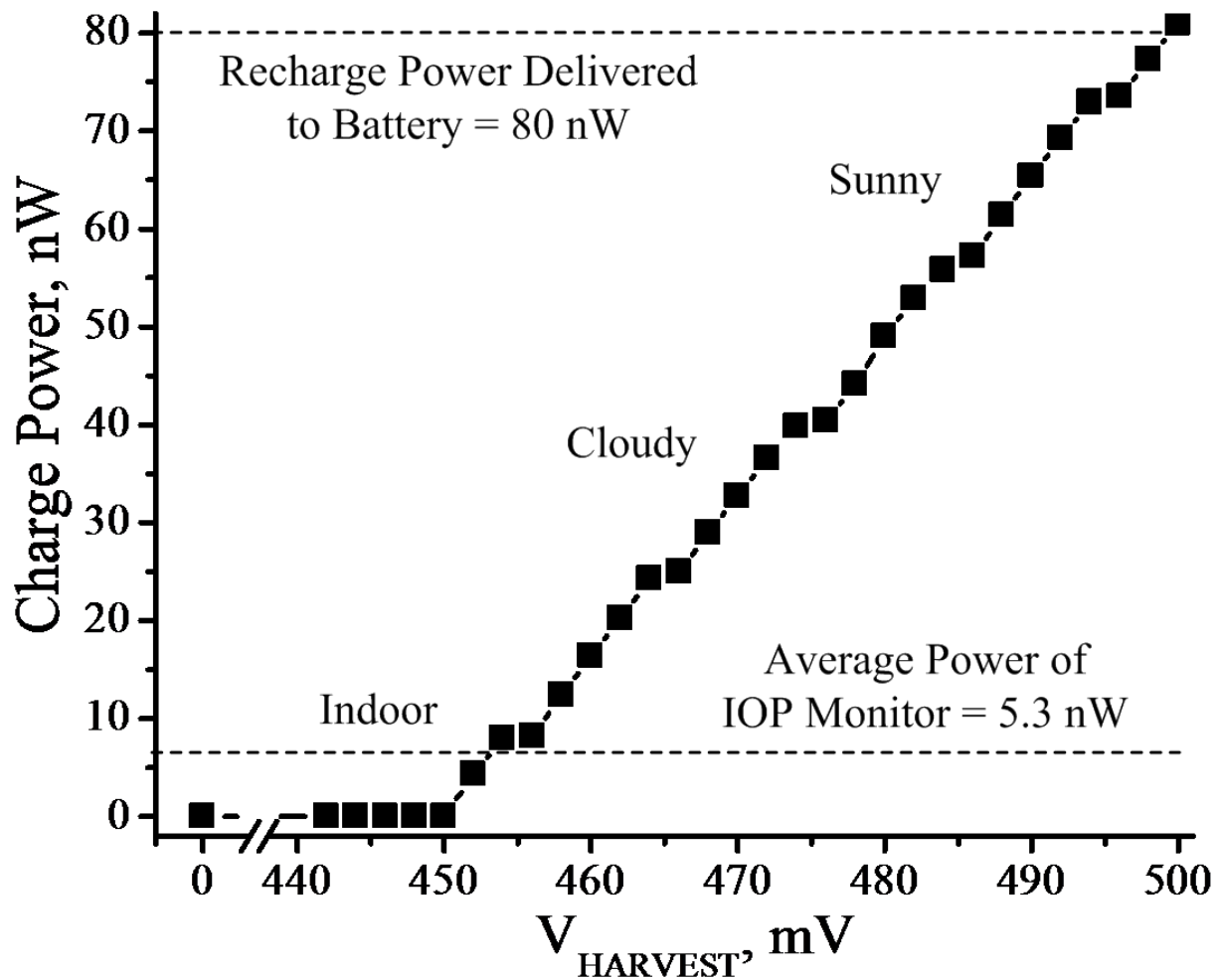
Figure 4.13: **The solar cells and switched capacitor voltage regulator deliver 80nW of power to recharge the battery.**

4.7 Summary

A 1.5 mm3 microsystem, targeted for minimally invasive implantation, measures IOP with an accuracy of 0.5 mmHg. Based on in vivo measurements, the transmitter wirelessly transmits measured pressure data through animal tissue to an external wand. It is designed to transmit data from within the eye to an external wand while consuming 4.7 nJ/bit, providing rapid IOP feedback to decrease physician response time for improved treatment. It harvests up to 80nW of solar power and uses ultra-low-power circuit techniques to achieve energy autonomy, extending lifetime indefinitely and potentially giving doctors time to converge upon the best glaucoma treatment. Energy-autonomous and nanowatt circuit techniques are needed to the enable cubic-millimeter microsystems that could eventually be used as part of future medical implants, such as blood pressure and glucose sensors, as well as non-medical devices, such as supply chain and infrastructure monitors.

CHAPTER 5

A 1.6nJ/bit, 19.9A Peak Current Fully Integrated 2.5mm^2 Inductive Transceiver for Volume-Constrained Microsystems

5.1 Motivation

Short communication range wireless sensor nodes are in great demand for intracranial [88], intraocular [40], and cardiac [89] applications, among others. One differentiating feature of such nodes is their highly miniaturized form factors [90], often in the mm range. As a result, the substantial work in low power RFID is incompatible with this emerging class of devices due to the large antennas of RFID card-type devices [91]. Current near-field solutions require large peak currents not feasible in such systems [92]. Very small (1-10mm^2) thin-film batteries offer the only reliable power source for such systems (Figure 5.1). While their 10-50mJ capacities are sufficient for the transmission of several Mb between battery recharges (at 1nJ/bit), their peak output current of 10-50μA is inconsistent with RF blocks (mA range). Therefore, these blocks must operate using a capacitive charge reservoir (nF range) that is recharged between radio transmissions. However, ms range recharge times reduce bit rate and place tighter requirements on timing reference jitter in order to maintain synchronization throughout the longer communication process. This in turn increases timing reference power (typically integrated on-chip), which can then come to dominate overall power consumption. Further, given the limited charge reservoir, the receiver start-up

58
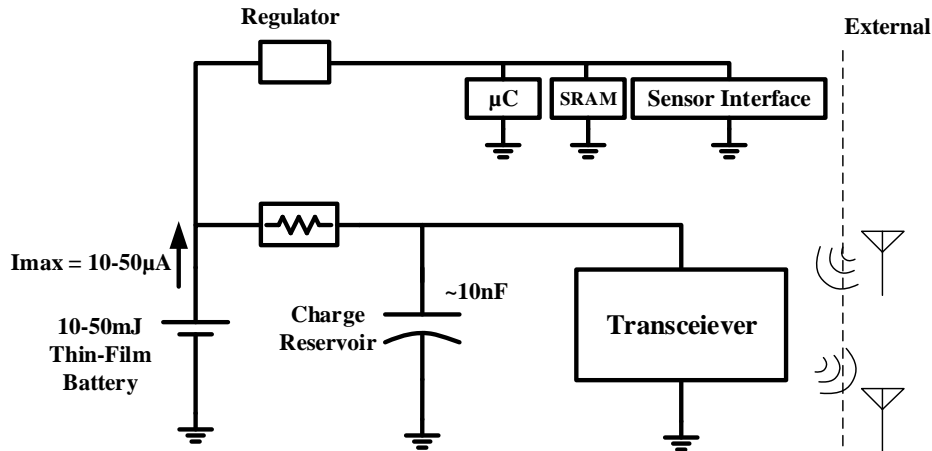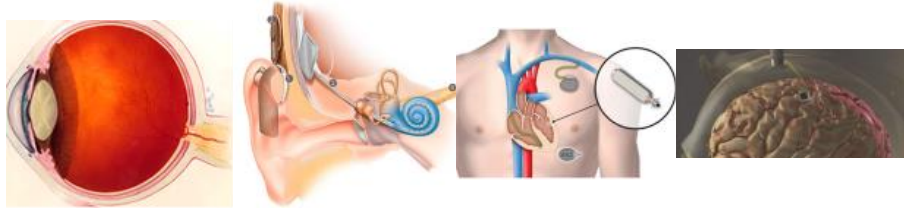
Figure 5.1: **Wireless integrated microsystems have myriad applications; one class of examples for highly miniaturized systems is implantable devices. The most practical power source for ultra-small wireless integrated microsystems is a 10-50mJ thin-film battery with limited peak current.**

time/energy becomes critical. Conventional methods with start-up times of 10 μs will fully deplete a 10nF capacitor at 5V (assuming a 5mA receiver).

To address this gap, we propose a $2.5mm^2$ near-field transceiver with integrated coils that uses a novel analog front-end and transmission protocol to relax synchronization requirements on the receive side (Figure 5.2). It uses a 14.3nF charge reservoir and requires 19.9uA peak current. The front-end uses a new fast-startup scheme to minimize start-up overhead and a new dual-coil LNA structure to maximize inductive coupling. The transceiver consumes 42.7nA during monitoring mode and 19.9 μA at 40.7kbps during active mode, drawn from a custom $2mm^2$ 3.6V thin-film battery suitable for 3D stacking with the radio die.
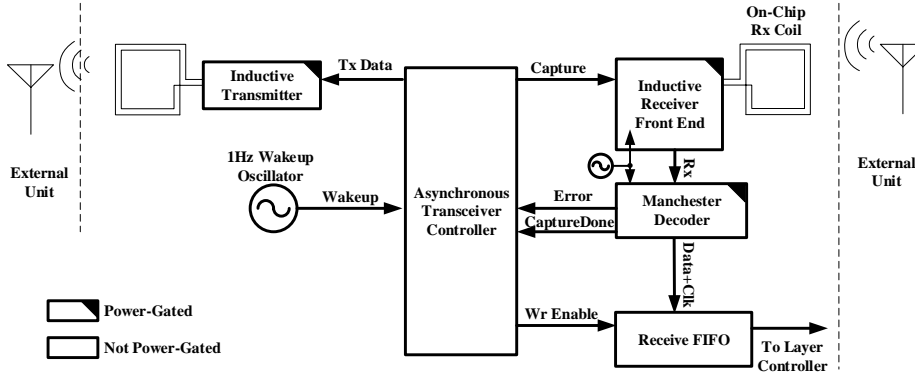
Figure 5.2: **The block diagram of the proposed transceiver is shown. An ultra-low leakage asynchronous controller coordinates transmit and receive operation and manages high-power blocks via power gating.**

5.2   Transceiver Protocol

The proposed CMOS transceiver consists of an asynchronous controller, a receiver front-end and decoder, and an inductive transmitter (5.2). To address the peak output current limitations of highly integrated microsystems, the transceiver uses a new half-duplex protocol that does not require accurate timing to receive data from an external unit (Figure 5.3). To initiate data transfer, the external unit sends out a beacon for 100ms, after which it ceases transmitting and listens for acknowledgement (Figure 5.3). The receiver is periodically woken up by a pW-level leakage-based oscillator. When activated during beaconing by the external unit, the receiver responds after a delay T_{wakeup} by sending an acknowledgement via its on-chip transmitter (tuned at the same frequency as the receiver to re-use spectrum). Next, the external unit starts data transmission by sending a payload packet (header + data) continuously (Figure 5.4). After recharging its charge reservoir, the receiver will wake up for a short period to capture the data and shut off immediately after its decoder extracts the Manchester-encoded data from the incoming stream. The decoder finds the beginning of the packet by locating the header and rotating the captured window.

By transmitting the same data many times from the external side, uncertainty in the capture window location becomes acceptable (Figure 5.3), which greatly relaxes constraints on clock jitter in the chip at the cost of increased power consumption in the external unit (typically not constrained). After receiving a packet, the receiver requests the next packet
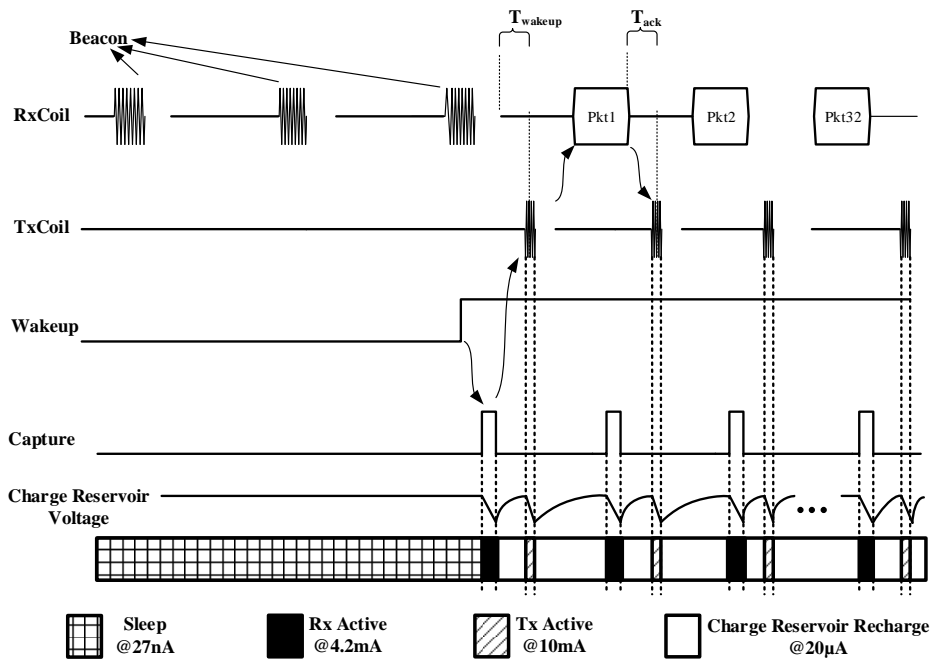
Figure 5.3: **The new transceiver protocol shifts link power and complexity to the external side, which has much less stringent energy constraints. The protocol allows the system to run off its MIM capacitor charge reservoir during active Rx and Tx modes and recharge its charge reservoir from the battery between packets while maintaining synchronization with the external unit.**
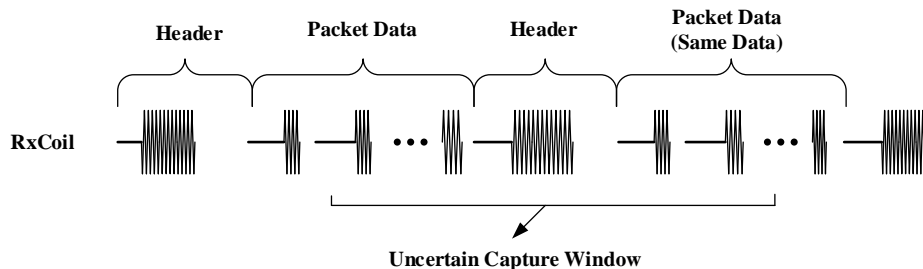
Figure 5.4: **Contents of a data packet. The packet includes 1-32 bits of data and a 4-bit header that are repeatedly sent by the external unit.**
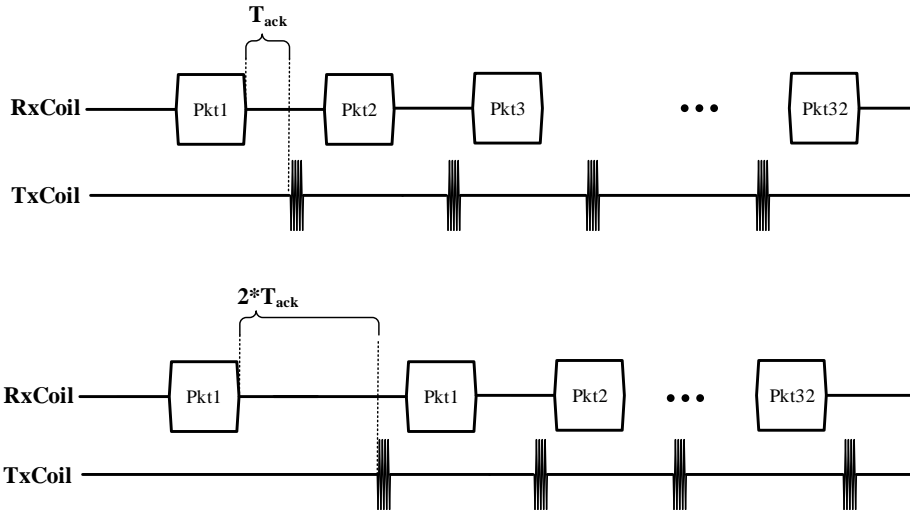
Figure 5.5: **The protocol has a mechanism to detect errors. The acknowledge sent to the external unit is delayed to notify the external unit of the unsuccessful reception.**

by sending a signal after a digitally tunable delay, T_{ack}, allowing time for the charge reservoir to recharge. If interference or noise cause the received bitstream to differ from the expected pattern, an acknowledgement is sent with a delay of $2T_{ack}$, signaling the external unit to retry the same packet (Figure 5.5). Data reception continues until the on-chip FIFO is full. Protocol timing is managed by the asynchronous controller (Figure 5.2), which is implemented using custom low-leakage high-Vth standard cells to limit total monitoring mode current to 42.7nA.

5.3   Receiver Front-End

Figure 5.6 shows the receiver front-end block diagram. The LNA amplifies and filter the voltage received from the external coil. The second stage further amplifies the signal and acts as a buffer for the filter. The filter removes all the noises from unwanted parts of the spectrum and delivers a clean signal to the final gain stage. The amplified signal is then fed to an envelope detector. The output of the envelope detector is compared with a dummy version of the same circuit to decide whether it corresponds to a zero or to a one. Block-level layout is optimized to ensure that any long wires appear at the output node of the LNA as
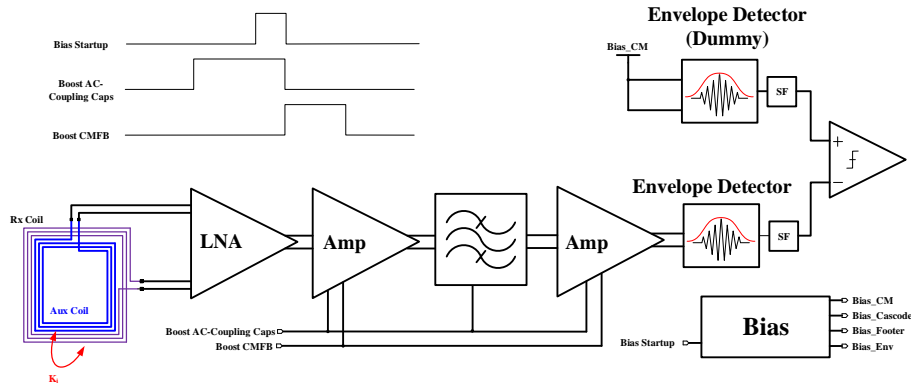
Figure 5.6: **Receive front-end block diagram.**

its tuned load absorbs parasitic capacitors.

A fully differential implementation maximizes immunity to interference and supply variation. Due to expected transient drops in the capacitive charge reservoir voltage, the entire front-end is designed to operate across $3 - 4.1V$. It consists of a cascode LNA using a 2-coil configuration, two amplifiers, a bandpass filter, two envelope detectors, and a clocked comparator preceded by a source follower. The dummy envelope detector experiences the same interference, supply, and process variation as the main envelope detector, thus improving power-supply rejection and variation immunity. The source follower attenuates clock kick-back from the comparator to the high-Z envelope detector output. The source-follower consumes only 10 μA, which is possible as the baseband signal is low frequency while the source-follower is inherently high frequency. When the front-end turns on (power gating released), startup switches short both plates of AC coupling capacitors to their steady-state values during the period shown in Fig. 3. After this, "Bias Startup" kick-starts bias circuitry to prevent unnecessary power consumption when front-end voltages are stabilizing. Finally, all common-mode feedbacks (CMFB) are boosted by injecting additional current to the error amplifiers until floating nodes approach their final values. Since transistors are not yet biased when CMFB boosting is asserted, instabilities caused by extra loop gain in CMFB are avoided. Using these techniques, receiver front-end start up time is reduced from 179 μs to 0.45 μs, rendering start-up energy less than 3% of total energy consumption for each received packet.

5.3.1 LNA

Unlike conventional antenna-driven LNAs, the inductive receiver uses an on-chip coil to couple to the external unit. Introducing a resistive input impedance by inductive degeneration would reduce the quality factor of our critical receive coil, degrading receive distance. To maximize mutual coupling between the on-chip coil and external unit, the inductor magnetic moment must be increased. Increasing area and/or number of turns can achieve this, however the correspondingly lower self-resonance-frequency (SRF) would cause the larger inductor to operate as a capacitor at the frequency of interest. Based on 3D EM simulations, 4-turn inductors are the largest possible that still enable 915MHz operation. Instead, we include a second 4-turn coil (Figure 5.7). This coil couples to the external coil in the same way as the main coil and is connected to the LNA cascode inputs ($k_{e,main}$ and $k_{e,aux}$ in Figure 5.7). When the auxiliary coil resonates, this approach provides extra feedback to the input by coupling to the main coil via k_i (≈ 0.6), enabling a 3.6dB frequency-selective gain improvement, translating to 22% added range (5.7). Since the high-gain (14.6dB) LNA dominates overall noise figure, subsequent blocks can exploit stacked transistors with CMFB to improve gain without affecting noise performance. The LNA amplifies the voltage received at two on-chip coils by effectively combining their received voltage with no power overhead and 11% area overhead compared to a single coil version.

5.3.2 Gain Stages

In order to maximize gain, the two gain stages in front-end of Figure 5.6 use a cascode structure with active load (Figure 5.8). Resistors are used instead of active loads to increase output resistance with only 250mV loss of headroom. This reduces the number of required bias voltages, enabling lower V_{dd} operation. All transistors, except for the input pair are high-V_t to be able to tolerate the 3.0-4.1V V_{dd} supplied by the thin-film Li-ion battery. Input differential pair, however, is not exposed to high voltages, which enables the nominal V_t transistors with higher transconductanc (g_m). Each gain stage provides 20dB of gain while consuming only $100\mu A$.
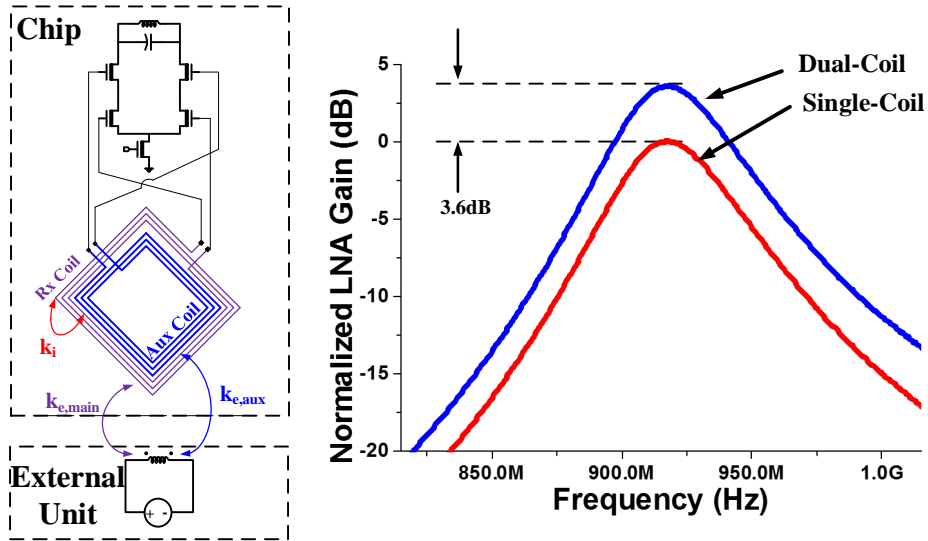
Figure 5.7: **Schematic and simulation results for the LNA. The LNA amplifies the voltage received at two on-chip coils by effectively combining their received voltage with no power overhead and 11% area overhead compared to a single coil version.**
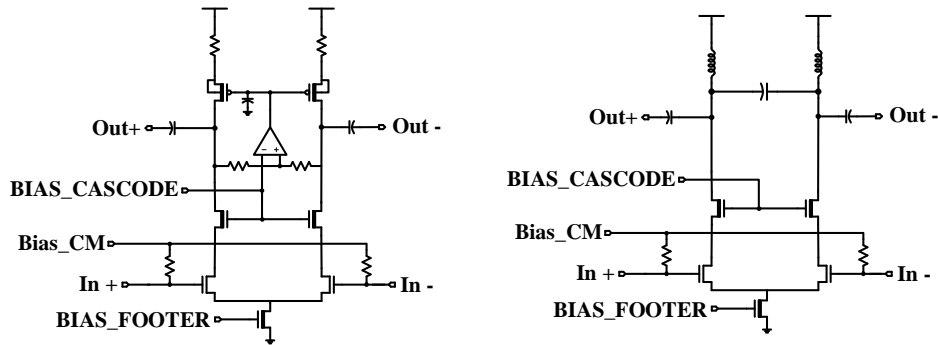
Figure 5.8: **Schematics for the gain stages and the filter.**

5.3.3 Filter

While LNA provides some frequency selectivity for the front-end, further filtering is required to attenuate the out-of-band components of the received signal. The filter achieves this goal by converting its input voltage into current and feeding the resulting current to a parallel LC tank (Figure 5.8). Tank frequency is digitally tunable from 890-940MHz. The cascode transistor improves bandwidth and avoids frequency pulling by the tuned load. This stage provides 5dB of gain while consuming only $200\mu A$ of current.
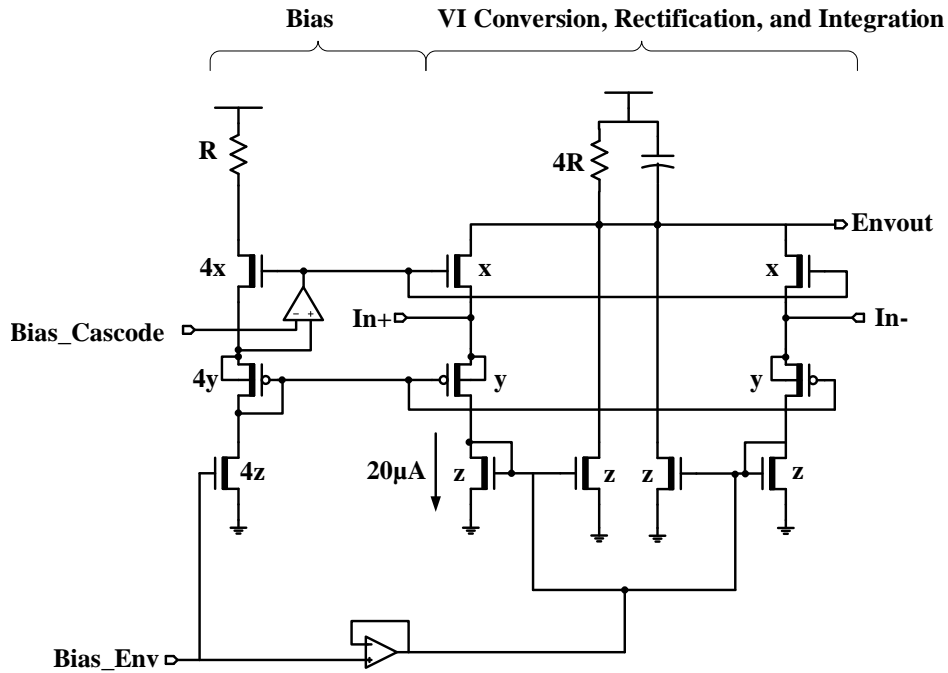
Figure 5.9: **Schematic of the integrating envelope detector.**

5.3.4 Envelope Detector

The envelope detector, first converts the input voltage to current (Figure 5.9). Then, it rectifies the currents during each half-cycles of the input signal's period. Finally, this current is integrated on a capacitor to generate the signal envelope. Since front-end is directly supplied by the 3.6V battery, we can use an efficient envelope detector architecture that has three transistors stacked on top of each other. The four rectifying branches of the envelope detector are biased at 20nA to minimize power. The envelope detector output is biased around V_{dd} to ensure proper bias during evaluation stage of the subsequent comparator. The envelope detector can pull down its output by 1.5V in $50\mu s$ with a 600mVp-p signal at its input.

5.3.5 Comparator

The comparator schematic shown in Figure 5.10. Amplification and evaluation are done using different differential pair to improve common-mode perforamance and input offset. The input-referred offset of all the transisors in the evaluation section of the circuit are divided
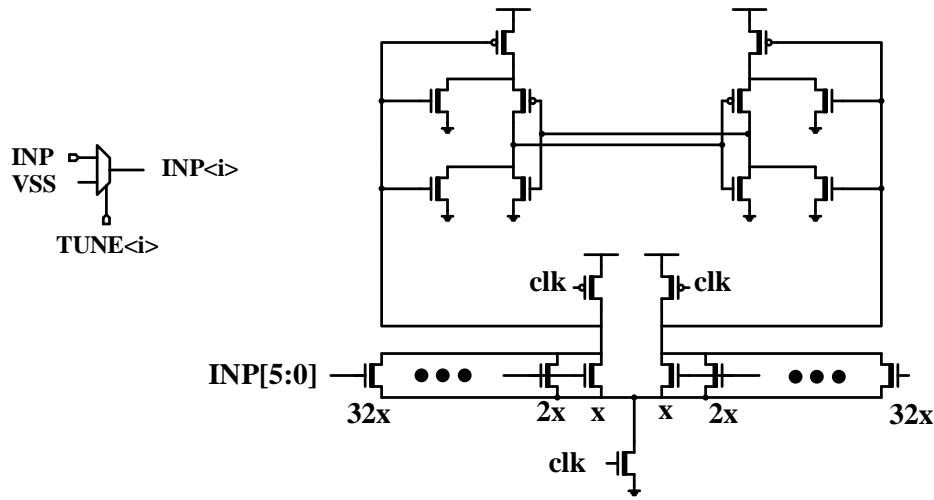
Figure 5.10: **Comparator schematic.**

by pre-amplifier gain, thus reducing overall offset. Comparator offset voltages as large as ± 3V are possible using digital tuning bits. Comparator consumes less than 100 μA when clocked at 20MHz.

5.4 Measurement Results

The transceiver is fabricated in $0.18\mu m$ CMOS and occupies $2.5mm^2$ core area. It consumes $71.6\mu W$ of active power at 40.7 kbps and reliably receives data from a 2W source positioned 1m away. The envelope detector output amplitude plots (Figure 5.11) show that the front-end chain can easily amplify signals at distances up to 1m. The transceivers two 1.7 x 1 mm coils have $Q \approx 4$ and provide sufficient magnetic moment to couple to transmitters up to 1m away. Figure 5.12 shows front-end and digital decoder active power at different receiver clock frequencies. Examining the active power breakdown, energy/bit becomes dominated by digital power at high bitrates, as expected. Figure 5.13 provides an oscilloscope shot of the wakeup-capture-capture-done sequence. Table 5.1 shows a comparison with recent inductive transceivers. The proposed inductive link achieves the highest reported receive range and level of integration in the literature. The chip micrograph is shown in Figure 5.14.
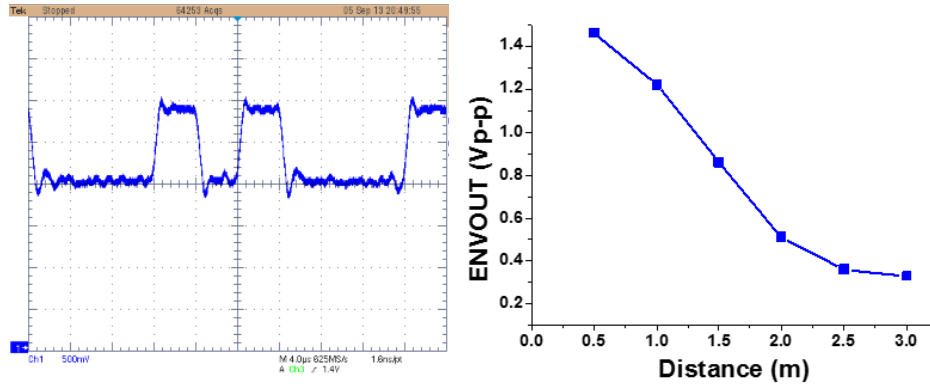
Figure 5.11: **Received peak-to-peak output as a function of distance and Sample oscilloscope shot of envelope detector output**
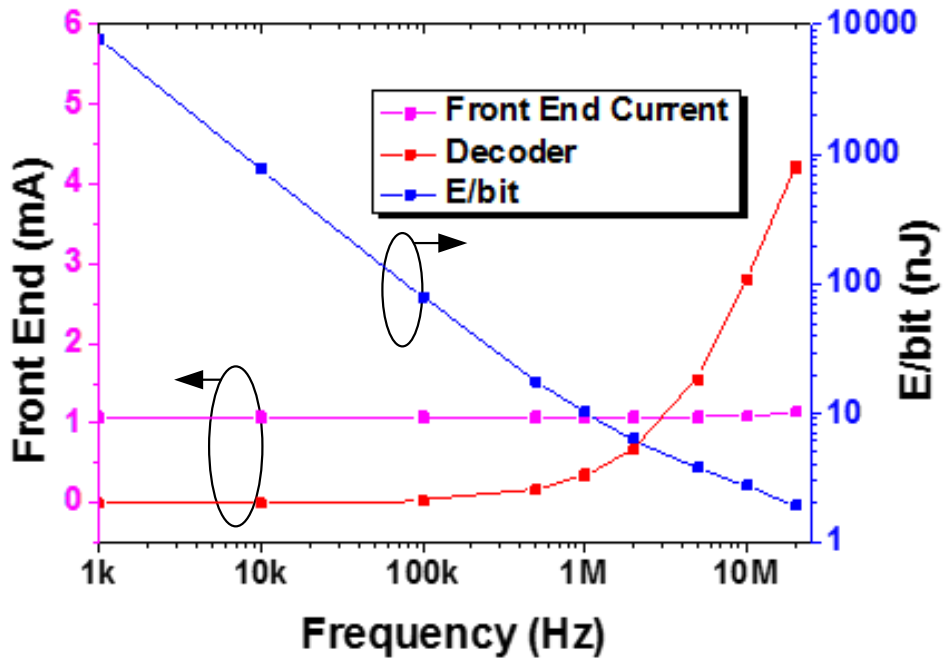
Figure 5.12: **Measured active power and energy per bit.**

Table 5.1: **Comparison with prior art in miniaturized inductive transceivers.**

	JSSC08 [93]	ISSCC11 [94]	ISSCC11 [40]	JSSC11 [95]	This Work
Modulation	DPSK	PSK	FSK	OOK	OOK
Carrier Frequency	20MHz	256kHz	915/433MHz	67.5MHz	915MHz
Energy per Bit	3.6nJ Rx	N/A	No Rx	0.29nJ Rx	1.6nJ Rx
	No Tx	N/A	4.7nJ Tx	0.34nJ Tx	4.7nJ Tx
Active Power	6.2mW@2Mbps	1.7μW^*	N/A	3mW@10.2Mbps	71.6 μW @ 40.7kbps
Rx Coil Location	Off-Chip	Off-Chip	On-Chip	Off-Chip	On-Chip
Rx Coil Max Dimention	22mm	20mm	0.5mm	15mm	1.7mm
Technology	0.35 μm	0.35 μm	0.18 μm	0.5 μm	0.18 μm
Receive Distance	1.5cm	1cm	0.4cm	1cm	100cm
Monitoring Mode Power	N/A	N/A	7 nW	N/A	153nW

68
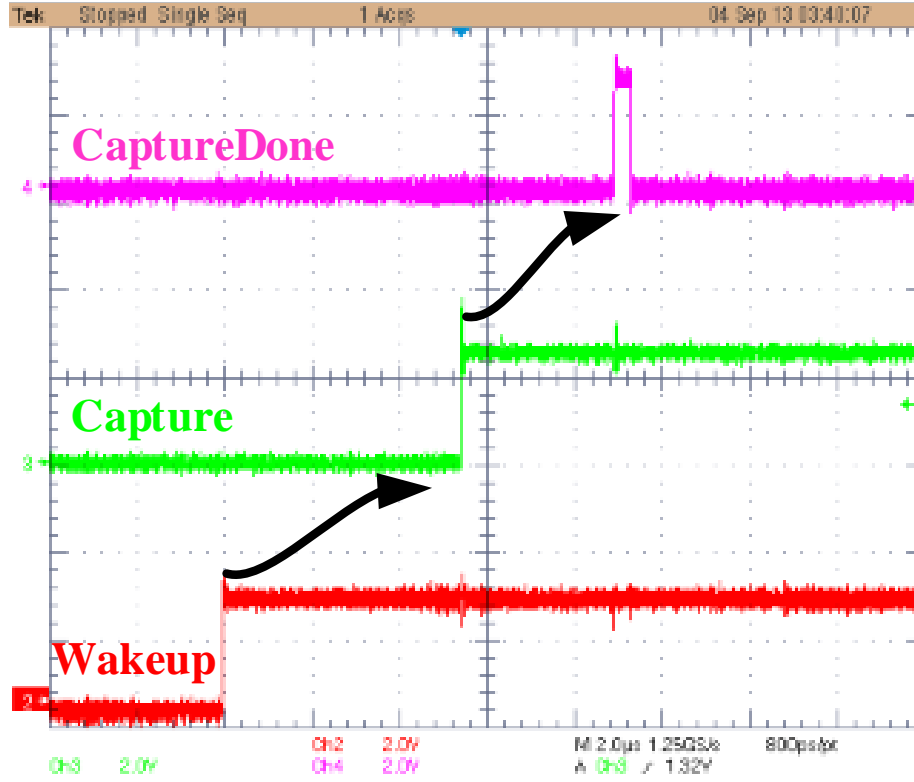
Figure 5.13: **Oscilloscope shot of system wakeup scheme.**
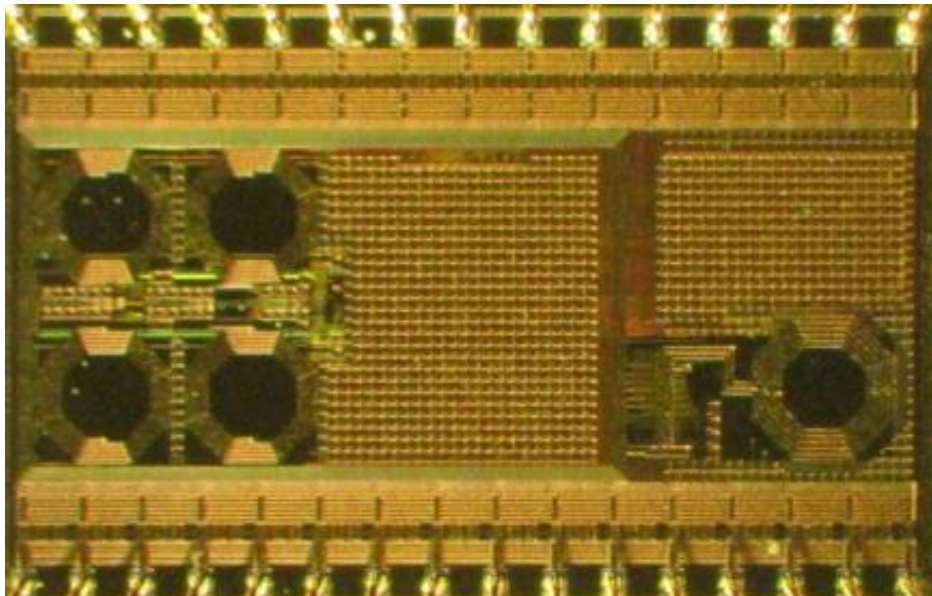
Figure 5.14: **Die micrograph of the transceiver in 180nm CMOS.**

CHAPTER 6

Conclusion and Future Directions

6.1 Conclusion

This work proposed solutions that help get one step closer to the goal of mm^3-sized computers. The work focuses on tackling different challenges that arise in design of implantable transceivers where system size and energy are highly limited. The transceiver proposed in this work was the first fully integrated mm^3 radio for biomedical implants that can achieve 1 meter of range while running off a mm^2 thin-film Li-ion battery.

Chapter 1 outlined the significance and motivation of the work. It clarified the reasons behind picking UHF band for through-tissue wireless transmission. It explains the major unresolved issues in miniature implantable wireless microsystems.

In Chapter 2 a model for stability of two-tone oscillators is derived. The model gives a lot of insight in different trade-offs when designing a double-tone FSK transceiver and enables us to minimize circuit power while maintaining low power levels.

Chapter 3 proposes a novel matching network for the receiver side of the wirelesss link. It explains why the implant transmitter will suffer from poor phase noise and how having a receiver that can detect two frequencies on the external side can be of immense help.

All the blocks required to build a complete mm^2 transceiver are put together in Chapter 4 to build an implantable biomedical microsystem. The microsystem is the first sensor node with such compact form-factor designed for continuous monitoring of intraocular pressure. The transceiver block was successfully implanted in live mouse tissue to prove the

functionality of the system.

Following the work on intraocular pressure monitoring microsystem, an improved transceiver with an active receive front-end and novel half-duplex protocol was presented in chapter 5. The inductive achieves the highest reported receive range (1m) in literature with all system components, including receive coil integrated on the $2.5mm^2$ chip.

6.2   Future Directions in Inductive Transceivers

Although the transceiver proposed in chapter 5 achieves the level of integration required for a complete microsystem, it is not exactly in the form factor that could be 3D-stacked with a processor and battery to form a complete system. Similar work that was done in [96] needs to be done to build a complete system. The commands that are currently scanned into the chip can come from a subthreshold processor layer that coordinates sensing, processing, charging. Extensive trials need to be done to make sure the thin-film battery can properly supply the system for hundreds of cycles. These cycles would involve sleep, wakeup-monitoring, pressure/temperature/pH sensing, data transmission, and reception of data from an external unit that, unlike the microsystem, is not energy-constrained.

Another option to explore is combining an RF harvesting unit with the transceiver. Previous work in this area relies on cm-size coils that would not fit within the form factor of most of our system [97]. By lowering average system power and optimizing the inductive link, an RF-powered microsystem will become feasible.

BIBLIOGRAPHY

[1] L.S.Y. Wong, S. Hossain, A. Ta, J. Edvinsson, D.H. Rivas, and H. Naas. A very low-power cmos mixed-signal ic for implantable pacemaker applications. *Solid-State Circuits, IEEE Journal of*, 39(12):2446–2456, 2004.

[2] K.C. Katuri, S. Asrani, and M.K. Ramasubramanian. Intraocular pressure monitoring sensors. *Sensors Journal, IEEE*, 8(1):12–19, 2008.

[3] A.M. Sodagar, G.E. Perlin, Y. Yao, K. Najafi, and K.D. Wise. An implantable 64-channel wireless microsystem for single-unit neural recording. *Solid-State Circuits, IEEE Journal of*, 44(9):2591–2604, 2009.

[4] M. Ashida, H. Majima, Y. Yoshihara, M. Nozawa, S. Oda, Y. Suzuki, J. Deguchi, H. Kobayashi, S. Kousai, R. Fujimoto, S. Ishizuka, T. Terada, S. Kawaguchi, Y. Unekawa, and M. Hamada. A 65nm cmos, 1.5-mm bluetooth transceiver with integrated antenna filter for co-existence with a wcdma transmitter. In *Solid State Circuits Conference (A-SSCC), 2012 IEEE Asian*, pages 81–84, 2012.

[5] S. Sen, F. Aryanfar, and C. Werner. A multiband transceiver system in 45-nm cmos for extended data rate through notchy wireline channels. *Circuits and Systems II: Express Briefs, IEEE Transactions on*, 58(9):545–549, 2011.

[6] Michael J McCullagh, David R Wisely, PL Eardley, and Peter P Smyth. A 50 mbit/s optical wireless lan link using novel optical and electronic enabling technologies. In *Mobile Communications Advanced Systems and Components*, pages 298–309. Springer, 1994.

[7] Alireza Zolfaghari and Behzad Razavi. A low-power 2.4-ghz transmitter/receiver cmos ic. *Solid-State Circuits, IEEE Journal of*, 38(2):176–183, 2003.

[8] Dongjin Oh, Minyeon Cha, Tae-Kyun Kim, and Ickjin Kwon. A fully integrated low-power 5-ghz cmos rf receiver for wlan applications. In *Proceedings of the 5th International Conference on Ubiquitous Information Management and Communication*, page 74. ACM, 2011.

[9] Nagendra Krishnapura, Majid Barazande-Pour, Qasim Chaudhry, John Khoury, Kadaba Lakshmikumar, and Akshay Aggarwal. A 5gb/s nrz transceiver with adaptive equalization for backplane transmission. In *Solid-State Circuits Conference, 2005. Digest of Technical Papers. ISSCC. 2005 IEEE International*, pages 60–585. IEEE, 2005.

[10] Udo Karthaus and Martin Fischer. Fully integrated passive uhf rfid transponder ic with 16.7-μw minimum rf input power. *Solid-State Circuits, IEEE Journal of*, 38(10):1602–1608, 2003.

[11] Zhicheng Lin, Pui-In Mak, and Rui Martins. A 1.7 mw 0.22 mm 2 2.4 ghz zigbee rx exploiting a current-reuse blixer+ hybrid filter topology in 65nm cmos. In *Solid-State Circuits Conference Digest of Technical Papers (ISSCC), 2013 IEEE International*, pages 448–449. IEEE, 2013.

[12] Rakesh Kumar, T Krishnaswamy, Gireesh Rajendran, Debapriya Sahu, Apu Sivadas, Murali Nandigam, Saravana Ganeshan, Srihari Datla, Anand Kudari, Hemant Bhasin, et al. A fully integrated 2× 2 b/g and 1× 2 a-band mimo wlan soc in 45nm cmos for multi-radio ic. In *Solid-State Circuits Conference Digest of Technical Papers (ISSCC), 2013 IEEE International*, pages 328–329. IEEE, 2013.

[13] A. Mirzaei, H. Darabi, A. Yazdi, Z. Zhou, E. Chang, and P. Suri. A 65 nm cmos quad-band saw-less receiver soc for gsm/gprs/edge. *Solid-State Circuits, IEEE Journal of*, 46(4):950–964, 2011.

[14] R Koller, T Ruhlicke, D Pimingsdorfer, and B Adler. A single-chip 0.13/spl mu/m cmos umts w-cdma multi-band transceiver. In *Radio Frequency Integrated Circuits (RFIC) Symposium, 2006 IEEE*, pages 4–pp. IEEE, 2006.

[15] Jongchan Kang, Ali Hajimiri, and Bumman Kim. A single-chip linear cmos power amplifier for 2.4 ghz wlan. In *Solid-State Circuits Conference, 2006. ISSCC 2006. Digest of Technical Papers. IEEE International*, pages 761–769. IEEE, 2006.

[16] Bernard Tenbroek, Jonathan Strange, Dimitris Nalbantis, Christopher Jones, Paul Fowers, Steve Brett, Christophe Beghein, and Federico Beffa. Single-chip tri-band wcdma/hsdpa transceiver without external saw filters and with integrated tx power control. In *Solid-State Circuits Conference, 2008. ISSCC 2008. Digest of Technical Papers. IEEE International*, pages 202–607. IEEE, 2008.

[17] King-Chun Tsai and Paul R Gray. A 1.9-ghz, 1-w cmos class-e power amplifier for wireless communications. *Solid-State Circuits, IEEE Journal of*, 34(7):962–970, 1999.

[18] Kouichi Kanda, Yoichi Kawano, Takao Sasaki, Noriaki Shirai, Tetsuro Tamura, Shigeaki Kawai, Masahiro Kudo, Tomotoshi Murakami, Hiroyuki Nakamoto, Nobumasa Hasegawa, et al. A fully integrated triple-band cmos power amplifier for wcdma mobile handsets. In *Solid-State Circuits Conference Digest of Technical Papers (ISSCC), 2012 IEEE International*, pages 86–88. IEEE, 2012.

[19] Nitz Saputra and John R Long. A fully-integrated, short-range, low data rate fm-uwb transmitter in 90 nm cmos. *Solid-State Circuits, IEEE Journal of*, 46(7):1627–1635, 2011.

[20] Eric Y Chow, Arthur L Chlebowski, and Pedro P Irazoqui. A miniature-implantable rf-wireless active glaucoma intraocular pressure monitor. *Biomedical Circuits and Systems, IEEE Transactions on*, 4(6):340–349, 2010.

[21] Y.S. Lin, D. Sylvester, and D. Blaauw. Near-field communication using phase-locking and pulse signaling for millimeter-scale systems. In *Custom Integrated Circuits Conference, 2009. CICC'09. IEEE*, pages 563–566. IEEE, 2009.

[22] Reid R Harrison, Ryan J Kier, Cynthia A Chestek, Vikash Gilja, Paul Nuyujukian, Stephen Ryu, Bradley Greger, Florian Solzbacher, and Krishna V Shenoy. Wireless neural recording with single low-power integrated circuit. *Neural Systems and Rehabilitation Engineering, IEEE Transactions on*, 17(4):322–329, 2009.

[23] Jun Ohta. Implantable cmos biomedical devices. In *Future of Electron Devices, Kansai (IMFEDK), 2012 IEEE International Meeting for*, pages 1–2. IEEE, 2012.

[24] John Louis Sommer, Scott J Brabec, Jon Frederic Urban, Yong-Fu Xiao, and Xiaohong Zhou. Implantable medical device for cardiac electrical stimulation, April 30 2010. US Patent App. 12/771,217.

[25] Tobi A Szuts, Vitaliy Fadeyev, Sergei Kachiguine, Alexander Sher, Matthew V Grivich, Margarida Agrochão, Pawel Hottowy, Wladyslaw Dabrowski, Evgueniy V Lubenov, Athanassios G Siapas, et al. A wireless multi-channel neural amplifier for freely moving animals. *Nature neuroscience*, 14(2):263–269, 2011.

[26] Makoto Saen, Kenichi Osada, Yasuyuki Okuma, Kiichi Niitsu, Yasuhisa Shimazaki, Yasufumi Sugimori, Yoshinori Kohama, Kazutaka Kasuga, Itaru Nonomura, Naohiko Irie, et al. 3-d system integration of processor and multi-stacked srams using inductive-coupling link. *Solid-State Circuits, IEEE Journal of*, 45(4):856–862, 2010.

[27] H.T. Friis. A note on a simple transmission formula. *proc. IRE*, 34(5):254–256, 1946.

[28] S. O'Driscoll, A. Poon, and T.H. Meng. A mm-sized implantable power receiver with adaptive link compensation. In *Solid-State Circuits Conference-Digest of Technical Papers, 2009. ISSCC 2009. IEEE International*, pages 294–295. IEEE, 2009.

[29] N. Miura, Y. Kohama, Y. Sugimori, H. Ishikuro, T. Sakurai, and T. Kuroda. An 11gb/s inductive-coupling link with burst transmission. In *Solid-State Circuits Conference, 2008. ISSCC 2008. Digest of Technical Papers. IEEE International*, pages 298–614. IEEE, 2008.

[30] D. Kurup, W. Joseph, G. Vermeeren, and L. Martens. Path loss model for in-body communication in homogeneous human muscle tissue. *Electronics letters*, 45(9):453–454, 2009.

[31] G. Simard, M. Sawan, and D. Massicotte. High-speed oqpsk and efficient power transfer through inductive link for biomedical implants. *Biomedical Circuits and Systems, IEEE Transactions on*, 4(3):192–200, 2010.

[32] K.S. Lee, H. Yu, H.K. Ahn, H.S. Oh, S. Ryu, D. Keum, and B.H. Park. A 0.13-μm cmos σ-δ frequency synthesizer with an area optimizing lpf, fast afc time, and a wideband vco for wcdma/gsm/gprs/edge applications. In *Radio Frequency Integrated Circuits Symposium, 2008. RFIC 2008. IEEE*, pages 299–302. IEEE, 2008.

[33] M. Shabany and P.G. Gulak. A 0.13 μm cmos 655mb/s 4× 4 64-qam k-best mimo detector. In *Solid-State Circuits Conference-Digest of Technical Papers, 2009. ISSCC 2009. IEEE International*, pages 256–257. IEEE, 2009.

[34] T. Ruhlicke, M. Zannoth, and B.U. Klepser. A highly integrated, dual-band, multi-mode wireless lan transceiver. In *Solid-State Circuits Conference, 2003. ESSCIRC'03. Proceedings of the 29th European*, pages 229–232. IEEE, 2003.

[35] L. Romano, V. Minerva, S.C. d'Oro, C. Samori, and M. Politi. 5-ghz in-phase coupled oscillators with 39% tuning range. In *Custom Integrated Circuits Conference, 2004. Proceedings of the IEEE 2004*, pages 269–272. IEEE, 2004.

[36] A. Goel and H. Hashemi. Frequency switching in dual-resonance oscillators. *Solid-State Circuits, IEEE Journal of*, 42(3):571–582, 2007.

[37] B. Van der Pol. The nonlinear theory of electric oscillations. *Proceedings of the Institute of Radio Engineers*, 22(9):1051–1086, 1934.

[38] N.M. Krylov and N.N. Bogoliubov. *Introduction to Non-Linear Mechanics.(AM-11)*, volume 11. Princeton University Press, 1949.

[39] D.B. Leeson. A simple model of feedback oscillator noise spectrum. *Proceedings of the IEEE*, 54(2):329–330, 1966.

[40] G. Chen, H. Ghaed, R. Haque, M. Wieckowski, Y. Kim, G. Kim, D. Fick, D. Kim, M. Seok, K. Wise, et al. A cubic-millimeter energy-autonomous wireless intraocular pressure monitor. In *Solid-State Circuits Conference Digest of Technical Papers (ISSCC), 2011 IEEE International*, pages 310–312. IEEE, 2011.

[41] B.U. Klepser, M. Punzenberger, T. Ruhlicke, and M. Zannoth. 5-ghz and 2.4-ghz dual-band rf-transceiver for wlan 802.11 a/b/g applications. In *Radio Frequency Integrated Circuits (RFIC) Symposium, 2003 IEEE*, pages 37–40. IEEE, 2003.

[42] J.L. Tham, M.A. Margarit, B. Pregardier, C.D. Hull, R. Magoon, and F. Carr. A 2.7-v 900-mhz/1.9-ghz dual-band transceiver ic for digital wireless communication. *Solid-State Circuits, IEEE Journal of*, 34(3):286–291, 1999.

[43] J.T. Kuo, T.H. Yeh, and C.C. Yeh. Design of microstrip bandpass filters with a dual-passband response. *Microwave Theory and Techniques, IEEE Transactions on*, 53(4):1331–1337, 2005.

[44] C. Quendo, E. Rius, and C. Person. An original topology of dual-band filter with transmission zeros. In *Microwave Symposium Digest, 2003 IEEE MTT-S International*, volume 2, pages 1093–1096. IEEE, 2003.

[45] P.R. Troyk and A.D. Rush. Inductive link design for miniature implants. In *Engineering in Medicine and Biology Society, 2009. EMBC 2009. Annual International Conference of the IEEE*, pages 204–209. IEEE, 2009.

[46] N.T. Tchamov, S.S. Broussev, I.S. Uzunov, and K.K. Rantala. Dual-band lc vco architecture with a fourth-order resonator. *IEEE Transactions on Circuits and Systems II: Express Briefs*, 54(3), 2007.

[47] R.M. Fano. Theoretical limitations on the broadband matching of arbitrary impedances. *Journal of the Franklin Institute*, 249(1):57–83, 1950.

[48] G.L. Matthaei, L. Young, and EMT Jones. *Microwave filters, impedance-matching networks, and coupling structures*, volume 1964. Artech House Dedham, MA, 1980.

[49] HA Quigley and AT Broman. The number of people with glaucoma worldwide in 2010 and 2020. *British Journal of Ophthalmology*, 90(3):262–267, 2006.

[50] P. Wong, C. Kania, M. Shah, P.R. Moinot, J. Schesser, W.C. Hunter, and T.L. Alvarez. Interfacing a tonometer with a microcontroller to monitor diurnal intraocular pressure variations. In *Bioengineering Conference, Proceedings of the 2010 IEEE 36th Annual Northeast*, pages 1–2. IEEE, 2010.

[51] M. Leonardi, P. Leuenberger, D. Bertrand, A. Bertsch, and P. Renaud. A soft contact lens with a mems strain gage embedded for intraocular pressure monitoring. In *TRANSDUCERS, Solid-State Sensors, Actuators and Microsystems, 12th International Conference on, 2003*, volume 2, pages 1043–1046. IEEE, 2003.

[52] K. Stangel, S. Kolnsberg, D. Hammerschmidt, BJ Hosticka, HK Trieu, and W. Mokwa. A programmable intraocular cmos pressure sensor system implant. *Solid-State Circuits, IEEE Journal of*, 36(7):1094–1100, 2001.

[53] P.J. Chen, D.C. Rodger, S. Saati, M.S. Humayun, and Y.C. Tai. Microfabricated implantable parylene-based wireless passive intraocular pressure sensors. *Microelectromechanical Systems, Journal of*, 17(6):1342–1351, 2008.

[54] Y.C. Shih, T. Shen, and B. Otis. A 2.3 μw wireless intraocular pressure/temperature monitor. In *Solid State Circuits Conference (A-SSCC), 2010 IEEE Asian*, pages 1–4. IEEE, 2010.

[55] EY Chow, S. Chakraborty, WJ Chappell, and PP Irazoqui. Mixed-signal integrated circuits for self-contained sub-cubic millimeter biomedical implants. In *Solid-State Circuits Conference Digest of Technical Papers (ISSCC), 2010 IEEE International*, pages 236–237. IEEE, 2010.

[56] RM Haque and KD Wise. A 3d implantable microsystem for intraocular pressure monitoring using a glass-in-silicon reflow process. In *Micro Electro Mechanical Systems (MEMS), 2011 IEEE 24th International Conference on*, pages 995–998. IEEE, 2011.

[57] RM Haque and KD Wise. An intraocular pressure sensor based on a glass reflow process. In *Solid-State Sensors, Actuators, and Microsystems Workshop*, pages 49–52, 2010.

[58] P. Riordan-Eva and J. Whitcher. *Vaughan & Asbury's general ophthalmology*. Wiley Online Library, 2008.

[59] M. Wieckowski, G.K. Chen, M. Seok, D. Blaauw, and D. Sylvester. A hybrid dc-dc converter for sub-microwatt sub-1v implantable applications. In *VLSI Circuits, 2009 Symposium on*, pages 166–167. IEEE, 2009.

[60] K. Tanaka, Y. Kuramochi, T. Kurashina, K. Okada, and A. Matsuzawa. A 0.026 mm¡ sup¿ 2¡/sup¿ capacitance-to-digital converter for biotelemetry applications using a charge redistribution technique. In *Solid-State Circuits Conference, 2007. ASSCC'07. IEEE Asian*, pages 244–247. IEEE, 2007.

[61] M. Elzakker, E. Tuijl, P. Geraedts, D. Schinkel, E.A.M. Klumperink, and B. Nauta. A 10-bit charge-redistribution adc consuming 1.9 μw at 1 ms/s. *IEEE Journal of Solid-State Circuits*, 45(5):1007–1015, 2010.

[62] J. O'Dowd, A. Callanan, G. Banarie, et al. Capacitive sensor interfacing using sigma-delta techniques. In *Sensors, 2005 IEEE*, pages 4–pp. IEEE, 2005.

[63] M. Bingesser, T. Loeliger, W. Hinn, J. Hauer, S. Mödl, R. Dorn, and M. Völker. Low-noise sigma-delta capacitance-to-digital converter for sub-pf capacitive sensors with integrated dielectric loss measurement. In *Proceedings of the conference on Design, automation and test in Europe*, pages 868–872. ACM, 2008.

[64] B. George and V.J. Kumar. Analysis of the switched-capacitor dual-slope capacitance-to-digital converter. *Instrumentation and Measurement, IEEE Transactions on*, 59(5):997–1006, 2010.

[65] Y. Chae and G. Han. A low power sigma-delta modulator using class-c inverter. In *VLSI Circuits, 2007 IEEE Symposium on*, pages 240–241. IEEE, 2007.

[66] S. Naraghi, M. Courcy, and M.P. Flynn. A 9b 14μw 0.06 mm 2 ppm adc in 90nm digital cmos. In *Solid-State Circuits Conference-Digest of Technical Papers, 2009. ISSCC 2009. IEEE International*, pages 168–169. IEEE, 2009.

[67] M. Shafahi and K. Vafai. Human eye response to thermal disturbances. *Journal of Heat transfer*, 133(1):11009, 2011.

[68] A. Wang, A.P. Chandrakasan, and S.V. Kosonocky. Optimal supply and threshold scaling for subthreshold cmos circuits. In *VLSI, 2002. Proceedings. IEEE Computer Society Annual Symposium on*, pages 5–9. IEEE, 2002.

[69] B.H. Calhoun and A. Chandrakasan. Characterizing and modeling minimum energy operation for subthreshold circuits. In *Low Power Electronics and Design, 2004. ISLPED'04. Proceedings of the 2004 International Symposium on*, pages 90–95. IEEE, 2004.

[70] B. Zhai, D. Blaauw, D. Sylvester, and K. Flautner. Theoretical and practical limits of dynamic voltage scaling. In *Proceedings of the 41st annual Design Automation Conference*, pages 868–873. ACM, 2004.

[71] J. Kwong, Y. Ramadass, N. Verma, M. Koesler, K. Huber, H. Moormann, and A. Chandrakasan. A 65nm sub-v¡ inf¿ t¡/inf¿ microcontroller with integrated sram and switched-capacitor dc-dc converter. In *Solid-State Circuits Conference, 2008. ISSCC 2008. Digest of Technical Papers. IEEE International*, pages 318–616. IEEE, 2008.

[72] S.C. Jocke, J.F. Bolus, S.N. Wooters, AD Jurik, AC Weaver, TN Blalock, and BH Calhoun. A 2.6-μw sub-threshold mixed-signal ecg soc. In *VLSI Circuits, 2009 Symposium on*, pages 60–61. IEEE, 2009.

[73] S. Hanson, M. Seok, Y.S. Lin, Z.Y. Foo, D. Kim, Y. Lee, N. Liu, D. Sylvester, and D. Blaauw. A low-voltage processor for sensing applications with picowatt standby mode. *Solid-State Circuits, IEEE Journal of*, 44(4):1145–1155, 2009.

[74] M. Seok, D. Sylvester, and D. Blaauw. Optimal technology selection for minimizing energy and variability in low voltage applications. In *Low Power Electronics and Design (ISLPED), 2008 ACM/IEEE International Symposium on*, pages 9–14. IEEE, 2008.

[75] G. Chen, M. Fojtik, D. Kim, D. Fick, J. Park, M. Seok, M.T. Chen, Z. Foo, D. Sylvester, and D. Blaauw. Millimeter-scale nearly perpetual sensor system with stacked battery and solar cells. In *Solid-State Circuits Conference Digest of Technical Papers (ISSCC), 2010 IEEE International*, pages 288–289. IEEE, 2010.

[76] J. Raszka, M. Advani, V. Tiwari, L. Varisco, ND Hacobian, A. Mittal, M. Han, A. Shirdel, and A. Shubat. Embedded flash memory for security applications in a 0.13 μm cmos logic process. In *Solid-State Circuits Conference, 2004. Digest of Technical Papers. ISSCC. 2004 IEEE International*, pages 46–512. IEEE, 2004.

[77] G. Chen, D. Sylvester, D. Blaauw, and T. Mudge. Yield-driven near-threshold sram design. *Very Large Scale Integration (VLSI) Systems, IEEE Transactions on*, 18(11):1590–1598, 2010.

[78] L. Chang, Y. Nakamura, RK Montoye, J. Sawada, AK Martin, K. Kinoshita, FH Gebara, KB Agarwal, DJ Acharyya, W. Haensch, et al. A 5.3 ghz 8t-sram with operation down to 0.41 v in 65nm cmos. In *VLSI Circuits, 2007 IEEE Symposium on*, pages 252–253. IEEE, 2007.

[79] N. Verma and A.P. Chandrakasan. A 65nm 8t sub-vt sram employing sense-amplifier redundancy. In *Solid-State Circuits Conference, 2007. ISSCC 2007. Digest of Technical Papers. IEEE International*, pages 328–606. IEEE, 2007.

[80] B.H. Calhoun and A. Chandrakasan. A 256kb sub-threshold sram in 65nm cmos. In *Solid-State Circuits Conference, 2006. ISSCC 2006. Digest of Technical Papers. IEEE International*, pages 2592–2601. IEEE, 2006.

[81] I.J. Chang, J.J. Kim, S.P. Park, and K. Roy. A 32 kb 10t sub-threshold sram array with bit-interleaving and differential read scheme in 90 nm cmos. *Solid-State Circuits, IEEE Journal of*, 44(2):650–658, 2009.

[82] D. Kim, G. Chen, M. Fojtik, M. Seok, D. Blaauw, and D. Sylvester. A 1.85 fw/bit ultra low leakage 10t sram with speed compensation scheme. In *Circuits and Systems (ISCAS), 2011 IEEE International Symposium on*, pages 69–72. IEEE, 2011.

[83] S. Mandal and R. Sarpeshkar. Power-efficient impedance-modulation wireless data links for biomedical implants. *Biomedical Circuits and Systems, IEEE Transactions on*, 2(4):301–315, 2008.

[84] G. Wang, W. Liu, M. Sivaprakasam, and G.A. Kendir. Design and analysis of an adaptive transcutaneous power telemetry for biomedical implants. *Circuits and Systems I: Regular Papers, IEEE Transactions on*, 52(10):2109–2117, 2005.

[85] A.C.W. Wong, D. McDonagh, G. Kathiresan, OC Omeni, O. El-Jamaly, T.C.K. Chan, P. Paddan, and AJ Burdett. A 1v, micropower system-on-chip for vital-sign monitoring in wireless body sensor networks. In *Solid-State Circuits Conference, 2008. ISSCC 2008. Digest of Technical Papers. IEEE International*, pages 138–602. IEEE, 2008.

[86] M.H. Ghaed, D. Sylvester, and D. Blaauw. A dual-passband filter architecture for dual-band systems. In *Antennas and Propagation (APSURSI), 2011 IEEE International Symposium on*, pages 3393–3396. IEEE, 2011.

[87] [46] Cymbet Corporation Rechargeable thin film battery 12Ah 3.8V datasheet®Technology. http://www.cymbet.com.

[88] Xu Meng, Usmah Kawoos, Shi-Min Huang, M-R Tofighi, and A Rosen. Implantable wireless devices for the monitoring of intracranial pressure. In *Consumer Electronics (ISCE), 2012 IEEE 16th International Symposium on*, pages 1–2. IEEE, 2012.

[89] Peng Cong, Nattapon Chaimanonart, Wen H Ko, and Darrin J Young. A wireless and batteryless 130mg 300μw 10b implantable blood-pressure-sensing microsystem for real-time genetically engineered mice monitoring. In *Solid-State Circuits Conference-Digest of Technical Papers, 2009. ISSCC 2009. IEEE International*, pages 428–429. IEEE, 2009.

[90] I-Ming Chen, Soo Jay Phee, Zhiqiang Luo, and Chee Kian Lim. Personalized biomedical devices & systems for healthcare applications. *Frontiers of Mechanical Engineering*, 6(1):3–12, 2011.

[91] D Yeager, Fan Zhang, Azin Zarrasvand, and Brian P Otis. A 9.2 μa gen 2 compatible uhf rfid sensing tag with- 12dbm sensitivity and 1.25 μvrms input-referred noise floor. In *Solid-State Circuits Conference Digest of Technical Papers (ISSCC), 2010 IEEE International*, pages 52–53. IEEE, 2010.

[92] Yogesh Darwhekar, Evgeniy Braginskiy, Koby Levy, Abhishek Agrawal, Vikas Singh, Ronen Issac, Ofer Blonskey, Ofer Adler, Yoav Benkuzari, Matan Ben-Shachar, et al. A 45nm cmos near-field communication radio with 0.15 a/m rx sensitivity and 4ma current consumption in card emulation mode. In *Solid-State Circuits Conference Digest of Technical Papers (ISSCC), 2013 IEEE International*, pages 440–441. IEEE, 2013.

[93] Mingcui Zhou, Mehmet Rasit Yuce, and Wentai Liu. A non-coherent dpsk data receiver with interference cancellation for dual-band transcutaneous telemetries. *Solid-State Circuits, IEEE Journal of*, 43(9):2003–2012, 2008.

[94] Shuenn-Yuh Lee, MY Su, Ming-Chun Liang, You-Yin Chen, Cheng-Han Hsieh, Chung-Min Yang, Hsin-Yi Lai, Jou-Wei Lin, and Qiang Fang. A programmable implantable microstimulator soc with wireless telemetry: Application in closed-loop endocardial stimulation for cardiac pacemaker. *Biomedical Circuits and Systems, IEEE Transactions on*, 5(6):511–522, 2011.

[95] Farzad Inanlou, Mehdi Kiani, and Maysam Ghovanloo. A 10.2 mbps pulse harmonic modulation based transceiver for implantable medical devices. *Solid-State Circuits, IEEE Journal of*, 46(6):1296–1306, 2011.

[96] Yoonmyung Lee, Suyoung Bang, Inhee Lee, Yejoong Kim, Gyouho Kim, Mohammad Hassan Ghaed, Pat Pannuto, Prabal Dutta, Dennis Sylvester, and David Blaauw. A modular 1 mm die-stacked sensing platform with low power i c inter-die communication and multi-modal energy harvesting. 2013.

[97] Mehdi Kiani and Maysam Ghovanloo. Pulse delay modulation (pdm) a new wideband data transmission method to implantable medical devices in presence of a power link. In *Biomedical Circuits and Systems Conference (BioCAS), 2012 IEEE*, pages 256–259. IEEE, 2012.